

---

# SCALABLE TEMPORAL ANOMALY CAUSALITY DISCOVERY IN LARGE SYSTEMS: ACHIEVING COMPUTATIONAL EFFICIENCY WITH BINARY ANOMALY FLAG DATA

---

A PREPRINT

 **Mulugeta Weldezigina Asres**

Centre for Artificial Intelligence Research  
University of Agder, Norway  
mulugetawa@uia.no

 **Christian Walter Omlin**

Centre for Artificial Intelligence Research  
University of Agder, Norway  
christian.omlin@uia.no

**The CMS-HCAL Collaboration**  
CERN, Switzerland

December 17, 2024

## ABSTRACT

Extracting anomaly causality facilitates diagnostics once monitoring systems detect system faults. Identifying anomaly causes in large systems involves investigating a more extensive set of monitoring variables across multiple subsystems. However, learning causal graphs comes with a significant computational burden that restrains the applicability of most existing methods in real-time and large-scale deployments. In addition, modern monitoring applications for large systems often generate large amounts of binary alarm flags, and the distinct characteristics of binary anomaly data—the meaning of state transition and data sparsity—challenge existing causality learning mechanisms. This study proposes an anomaly causal discovery approach (ANOMALYCD), addressing the accuracy and computational challenges of generating causal graphs from binary flag data sets. The ANOMALYCD framework presents several strategies, such as anomaly flag characteristics incorporating causality testing, sparse data and link compression, and edge pruning adjustment approaches. We validate the performance of this framework on two datasets: monitoring sensor data of the readout-box system of the Compact Muon Solenoid experiment at CERN, and a public data set for information technology monitoring. The results demonstrate the considerable reduction of the computation overhead and moderate enhancement of the accuracy of temporal causal discovery on binary anomaly data sets.

**Keywords** Causal Discovery · Root Cause Analysis · Anomaly Detection · Binary Data · Compact Muon Solenoid

## Acronyms

<b>AD</b>	Anomaly Detection	<b>CP</b>	Conditional Probability
<b>ANAC</b>	Our Anomaly Aware CI Test	<b>CPD</b>	Conditional Probability Distributions
<b>ANOMALYCD</b>	Our Anomaly CD Approach	<b>DAG</b>	Directed Acyclic Graph
<b>APRC</b>	Area Under the Precision-Recall Curve	<b>DL</b>	Deep Learning
<b>BN</b>	Bayesian Network	<b>DQM</b>	Data Quality Monitoring
<b>CD</b>	Causal Discovery	<b>FCI</b>	Fast Causal Inference
<b>CI</b>	Conditional Independence	<b>FCM</b>	Functional Causal Model
<b>CMS</b>	Compact Muon Solenoid	<b>FFT</b>	Fast Fourier Transform

Source code: <https://github.com/muleina/AnomalyCD>

<b>GAE</b>	Graph Autoencoder	<b>PC</b>	Peter-Clark
<b>GCM</b>	Causal Graph Model	<b>PCMCI</b>	Peter-Clark Momentary CI
<b>GES</b>	Greedy Equivalent Search	<b>PDAG</b>	Partial Directed Acyclic Graph
<b>GFCI</b>	Greedy Fast Causal Inference	<b>QIE</b>	Charge Integrating and Encoding
<b>GS</b>	Grow-Shrink	<b>RBX</b>	Readout Box
<b>HCAL</b>	Hadron Calorimeter	<b>RCA</b>	Root-Cause Analysis
<b>HE</b>	HCAL Endcap Detector	<b>RM</b>	Readout Module
<b>HEM</b>	HE Minus Hemisphere RBX	<b>SHD</b>	Structural Hamming Distance
<b>HEP</b>	HE Plus Hemisphere RBX	<b>SHDU</b>	Undirected SHD
<b>IAMP</b>	Incremental Association	<b>SiPM</b>	Silicon Photomultipliers
<b>LHC</b>	Large Hadron Collider	<b>TPC</b>	Time-Aware PC
<b>MMHC</b>	Max-Min Hill Climbing	<b>TS</b>	Time Series
<b>MMPC</b>	Max-Min Parents and Children	<b>VTTx</b>	Versatile Twin Transmitter

## 1 Introduction

Anomaly detection (AD) approaches are commonly employed in industrial monitoring systems to capture anomalies that require attention to improve efficiency, safety, and reliability while reducing maintenance expenses [1, 2]. Discovering causality from a broader range of sensors, including variables not monitored by pre-trained AD models, for captured anomalies is essential to facilitate fault diagnostics through root cause discovery and analysis. Causal knowledge of direct and indirect effects, interaction pathways, and time-lags can assist in comprehending the fault nature and modeling physical systems to predict the impact of anomaly occurrence or interventions [3].

The propagating nature of malfunctions makes fault diagnosis challenging in most multivariate processes [1]. Causal knowledge of faults is traditionally acquired through inductive and deductive risk analysis using variants of failure mode and effects analysis, and fault tree analysis, respectively [4]. These approaches provide rules for modeling expert knowledge for prior known malfunctions; they may also incorporate querying mechanisms [5]. The approaches require extensive domain knowledge from many experts and are a time-consuming process in addition to the possible ambiguity and incompleteness in large systems [4]. Data-driven approaches directly learn causality from the data collected by the sensor monitoring systems [1, 6–12]. AD and causal discovery (CD) often remain highly intractable due to widely diverse operational modes, disparate data types, and complex fault propagation mechanisms [2, 7, 8]. Recent advances in AD for large complex systems focus on specific subsystems because of the curse of dimensionality, data annotation challenges, and the need for accuracy improvement; this results in multiple AD models for monitoring different subsystems [13–19]. Identifying the causes of an anomaly requires investigating an extensive set of monitoring variables across subsystems that the trained AD models may not cover. An end-to-end framework for anomaly CD that addresses the challenges pertaining to large systems is thus of interest in various domains.

We propose an anomaly causal discovery framework (ANOMALYCD) consisting of several methods to address various challenges related to generating causal knowledge discovery on multivariate anomaly data. We employ anomaly alert aggregation from multiple systems ameliorated with a temporal online AD method, sparse data handling, causal graph structure learning, and causality inference with Bayesian network modeling. Our study focuses on discovering anomaly causality from time series (TS) binary flags. Binary flag data lessens the impact of data heterogeneity streamed from diverse AD models, and provides data normalization. Although there are some recent efforts for inferring empirical causal graphs from binary data [20] or outlier signals [21], there is still a gap in addressing the unique challenges of binary anomaly data for large systems. Time series binary anomaly data has distinctive characteristics different from ordinary categorical or discrete data: 1) flag transitions between normal 0 and alert 1 have a meaning of anomaly occurrence and disappearance, and 2) data may exhibit severe data sparsity because of long uniform status regimes. The existing causality learning mechanisms have yet to be established effectively to handle these characteristics. We present a customized conditional independence (CI) test to incorporate the anomaly data attributes, a Peter-Clark momentary CI (PCMCI) algorithm—a popular constraint-based estimator for CD on TS data [22–25])—to generate the anomaly causal graph structure, and Bayesian network [26] to query causality inference. We also propose a simple but promising compression method for binary anomaly-flag data that substantially reduces the computational load of the causal graph learning process. We have applied the proposed framework to monitor multivariate sensor data from the readout box systems of the Hadron Calorimeter (HCAL) of the Compact Muon Solenoid (CMS) experiment at CERN’s Large Hadron Collider (LHC). The results establish that our approach accurately detects outlier behaviors and generates causal networks consistent with the actual physical circuit connections and environmental associations. We have assessed and compared the efficacy of our approach with the performance of popular CD methods on a publically available information technology infrastructure monitoring dataset. The proposed ANOMALYCD approach improves the causal

graph accuracy and considerably the computational efficiency of graph learning. Moreover, we have conducted an ablation study on ANOMALYCD to demonstrate the contribution of the proposed techniques.

We discuss the background on CD in Section 2. We briefly describe the HCAL readout box system and the monitoring sensor data sets employed in the study in Section 3. We present our approaches in Section 4, and provide results and discussion in Section 5. We summarize the contribution of our study in Section 6.

## 2 Background

In this section, we will discuss background concepts and review recent studies on causal graph learning for TS data.

### 2.1 Anomaly Causal Discovery and Analysis

In the realm of system monitoring for complex systems, it is imperative to delve beyond predictive or descriptive machine learning tasks to fully comprehend the cause-effect relationship among different variables and systems [7, 8]. The investigation of causality is a prominent area of interest in diverse fields, including but not limited to IT systems [27, 28], transportation [4], medical science [29, 30], meteorology [7], and social science [20]. Causal presentation of multivariate is an essential component in root-cause analysis (RCA) that deals with the identification of the underlying root causes and provides an explanation of how the faults are impacting the monitored system [21, 28, 31]. Models of causal relationships may answer additional diagnostic questions, such as what would happen if faults occur in particular variables and predicting how specific variables trigger faults in other variables or systems. Causal discovery and analysis are becoming increasingly essential in the industry for identifying the underlying behaviors and evolution of process faults [6, 7]. The relationship among different variables or components often involves multiple time lags in modern cyber-physical industrial systems. These time lags delay the fault propagation on the causally connected process variables [32]. Although temporal data provides valuable context that enhances AD and CD, it requires special handling to address the specific challenges often posed by the temporal data characteristics or the complexity of causal processes emanating from slower data acquisition rates than the underlying rate of changes, missing data, measurement error, non-stationarity, unmeasured confounding factors, and causality heterogeneity and non-linearity (concept drift on the causal relationship) [6, 7].

Here we discuss some of the recent data-driven approaches for CD and RCA, which include statistical [1, 10, 33–36], information theory [1], and machine learning algorithms [2, 8, 12, 32, 33]. Rashidi et al. [1] present kernel principal component analysis (KERNEL-PCA) transformation and symbolic transfer entropy to reduce causality analysis computation for RCA fault diagnosis on multivariate nonlinear variables. The residual data of KERNEL-PCA detects system faults, and normalized transfer entropy determines the causal pathways from process variables to the residual signal. The proposed method identifies only potential root causes and does not provide causal interactions among TS variables. Tian et al. [10] propose convergent cross-mapping to build a causal network for TS alarm data root cause tracing in industrial processes. The study assumes only deterministic system theory that the data is a chaotic TS generated by a nonlinear deterministic system. Chen et al. [33] combine multivariate nonlinear chirp mode decomposition with Granger causality to detect and analyze root causes for multiple plant-wide oscillations in a process control system. The approach involves oscillating variable clustering and Granger causality to each group to obtain the root causes. Liu et al. [8] employ a spatio-temporal pattern network for RCA on TS anomalies in distributed complex systems. The anomalies are detected from changes in the causality dependency networks generated from a restricted Boltzmann machine model trained on symbolic representation of the healthy TS data. The energy strength of switching or flipping a symbolic pattern indicates potential root causes. Steenwinckel et al. [4] discuss fusing expert knowledge with a data-driven semantic rule mining for adaptive AD and RCA for predictive maintenance of trains. They employ matrix profiling [36], a sliding time window pattern matching through z-normalized Euclidean distance, to find abnormal discords in sensors and match incoming patterns against those previously confirmed anomalies. Liu et al. [35] discuss fine-tuning Spearman’s rank correlation analysis with domain knowledge rules to build a Bayesian network for fault detection and diagnosis. Qin et al. [34] utilize PCA-based fault detection and variable selection using feature importance from extreme gradient boosting for RCA. The study adopts the temporal CD network from [11] to analyze the root cause of faults without historical fault information. Leonhardt et al. [2] employ deep graph convolution neural networks to solve the sparse and nonlinear problem of the state space models for RCA.

Recent approaches have also integrated causality inference into the AD deep learning models [12, 32]. Zhou et al. [12] present a framework using temporal convolution and multi-head self-attention networks for CD and a contrastive causal graph for RCA in multivariate TS. They propose modifying the convolutional neural networks with feature reconstruction and skip connections to improve feature extraction and detect delay-time causalities. Their attention method employs threshold normalization for quantifiable causal inference. Chen et al. [32] propose a sparse causal residual neural network model to extract multi-time-lag causality for industrial process fault diagnosis. The model’s

parameters describe the integral causal structure by optimizing a multivariate TS forecasting objective with hierarchical sparsity constraints.

Causal graph networks are popular for their intuitive presentation capability [21, 27, 31, 37]; they provide a visual presentation of the causality using graphs. The graphs show influence and effect paths, provide strength and direction of leakage, and allow calculation of influence propagation on the paths; these attributes make causal graphs popular for identifying the CD and RCA applications [21, 31]. Wang et al. [27] presents CLOUDRANGER that utilizes the non-temporal Peter-Clark (PC) algorithm for TS data to discover the causal graph between anomalies and identifies root causes through a random walk on a transition matrix. They employ correlation between variable pairs to generate the transition matrix. MICROCAUSE in Ref. [28] enhances the CLOUDRANGER by inferring the causal graph discovery using the PCMI algorithm [23]. The MICROCAUSE estimates the partial correlation between causally related variables given their parents in the graph to compute the transition matrix for the random walk. WHYMDC in Ref. [37] identifies root causes from non-temporal data by searching for changes in causality on a given directed acyclic causal graph. CAUSALRCA in Ref. [21] employs the SHAPLEY value [38] to quantify contributions and rank root causes of a point anomaly score using non-temporal structural causal models. EASYRCA in Ref. [31] identifies the root causes of collective anomalies in TS data from an acyclic causal graph. The approach utilizes a summary causal graph (without time lag specification) of the TS data in a normal operation. The root causes are captured for each group either directly from the graph and appearance time of the anomalies or by comparing causal effects in the normal and abnormal regimes. The study does not address the problem of causal graph discovery, and it assumes that the graph already exists, which is a challenging assumption to hold in several real-world complex systems. The above recent approaches for anomaly RCA are not adequately optimized for binary anomaly-flag data CD, as the methods are limited to non-temporal modeling or prerequisite on the availability of the causal network [21, 27, 31, 37]. Large complex systems often exhibit temporal fault propagation, the actual fault causal network is not readily available as the number of variables grows, and the fault network might differ from normal operation casual networks.

## 2.2 Causal Graph Discovery Methods

The first step of graph-based causality analysis is to construct the causal graph model of the variables (see Definition 1). The graph model captures direct dependencies and shared drivers among multiple data variables, the graph nodes.

**Definition 1** *Graphical causal model (GCM) states that if two variables have an edge in between  $X \rightarrow Y$  in the directed graph, then  $X$  is a direct cause of  $Y$ ; there exist interventions on  $X$  that will directly change  $Y$  (distribution or value). The edge of GCM between variables  $X$  and  $Y$  can model 1) a direct causal relationship ( $X \rightarrow Y$  or  $Y \rightarrow X$ ), 2) a causal relationship in either direction ( $X \leftrightarrow Y$ ), and 3) a non-causal association ( $X \leftrightarrow Y$ ) due to external common causes.*

Data-driven causal graph structure learning methods can broadly be categorized into:

- *Constraint-based*: Relies on conditional independence (CI) relationships  $X \perp Y | Z$  ( $X$  independent of  $Y$  condition on  $Z$ ) to infer the causal directed acyclic graph (DAG) structure. Some of the popular methods include PC [29], grow-shrink (GS) [39], incremental association (IAMP) [40], max-min parents and children (MMPC) [41], and fast causal inference (FCI) [29]). The PC algorithm in Refs. [29, 42] is a widely used method that builds a causal graph by adding edges based on CI tests. It learns a partial DAG (PDAG) representing the dependencies based on the causal Markov condition and faithfulness assumption. When there is no latent confounder, two variables are directly causally related with an edge in between if and only if there is no subset of the remaining variables conditioning on which they are independent. Three main steps are involved in the PC: 1) identifying the graph skeleton induced by those CI relations, 2) identifying v-structure ( $X \rightarrow Y \leftarrow Z$ ), and 3) deriving edge directions. FCI [29] loosens the causal sufficiency assumption—the measured variables include all common causes, and there is no unobserved confounding variable—of PC to deal with unmeasured latent variables.
- *Score-based*: Employs optimization search for causal DAG structure to the observed data based on a scoring metric [3, 6, 7, 43]; e.g., hill-climbing search (HC) [44], and greedy equivalent search (GES) [45, 46]. These methods explore the space of PDAGs structure classes and minimize a global score—e.g., the *Bayesian information criterion* and *Bayesian Dirichlet equivalent uniform prior*—using add, remove, and reverse edge operators to return the optimal structure [45, 46].
- *Hybrid*: Combines the ideas from constraint-based and score-based algorithms to enhance accuracy and computational efficiency; e.g., max-min hill climbing (MMHC) [43], and greedy FCI (GFCI) [47]. MMHC algorithm first builds the skeleton network using CI tests and then performs a Bayesian-scoring greedy HC to orient the edges [43]. Greedy FCI embarks with fast GES to get a first sketch of the graph rapidly, then uses the FCI constraint-based rules to orient the edges in the presence of potential confounders [47].

- *Functional causal model (FCM)*: is a recent CD approach that represents the effect as a function of the causes and independent noise terms [43, 47]; e.g., causal additive models [48] and causal generative neural networks [49] and others [6, 7]. FCM captures the asymmetry between cause and effect variables, representing the effect  $Y$  as a function of the direct causes  $X$  and noise factor  $\vartheta$  as:

$$Y \leftarrow f_{\theta}(X, \vartheta; \theta) \quad (1)$$

where  $\vartheta$  is the noise term that is assumed to be independent of  $X$ , the function  $f$  explains how  $Y$  is generated from  $X$ , and  $\theta$  is the parameter set of  $f$ . Diverse FCM approaches have been proposed in the literature using regression models, structural equation models, autoregressive models, and neural network models as reviewed in Refs. [6, 7].

Structured reviews on learning methods for GCM are available in Refs. [6, 7], and a more detailed explanation of structural causal model properties in a textbook [50]. We limit our discussion to studies related to TS data as in Refs. [3, 11, 12, 22–25, 32, 51–53].

### 2.2.1 Causal Discovery in Time Series Data

Causal graph modeling for TS data is a growing study area in several scientific disciplines [22, 51]. Multivariate TS data become abundant in several real-world domains with the proliferation of the sensor networks, but finding the causal dynamics in such data is challenging for many reasons: non-linearity of the generating process, data non-stationarity, concept drift over time, varying data rates, and missing data [6]. Time series GCM approaches need to capture time-lag causality besides addressing the stated challenges of TS data (see Figure 1). Commonly employed TS GCM methods include Granger causality [51, 52], constraint-based [3, 3, 22–25, 53], and machine learning [11, 12, 32].

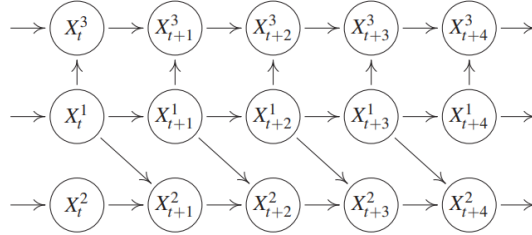


Figure 1: A TS with time lag effect  $\mathbf{x}_{t-1}^1 \rightarrow \mathbf{x}_t^2$  and instantaneous effect  $\mathbf{x}_t^1 \rightarrow \mathbf{x}_t^3$  [50].

A popular method for TS data is the Granger causality [54] that formulates a notion of causality based on how well past values of a TS  $\mathbf{y}_t$  could predict future values of another series  $\mathbf{x}_t$ . Let  $\mathcal{H}_{<t}$  be all the relevant history information up to time  $t - 1$  and  $f(\mathbf{x}_t | \mathcal{H}_{<t})$  be the optimal prediction of  $\mathbf{x}_t$  given  $\mathcal{H}_{<t}$ . Granger defined  $\mathbf{y}$  to be causal for  $\mathbf{x}$  if:

$$\text{var}[\mathbf{x}_t - f(\mathbf{x}_t | \mathcal{H}_{<t})] < \text{var}[\mathbf{x}_t - f(\mathbf{x}_t | \mathcal{H}_{<t}/\mathbf{y}_{<t})] \quad (2)$$

where  $\text{var}$  denotes variance, and  $\mathcal{H}_{<t}/\mathbf{y}_{<t}$  indicates excluding the values of  $\mathbf{y}_{<t}$  from  $\mathcal{H}_{<t}$ . Granger assumes the identifiability of a unique linear model with  $N$  TS variables as:

$$\mathbf{x}_t^i = \sum_{s=1}^q A_s^{ij} \mathbf{x}_{t-s}^j + \mathbf{e}_t^i, \quad \forall j \neq i \quad (3)$$

where  $A^1, \dots, A^{N-1}$  are  $N \times q$  lag coefficient matrices with order  $N - 1$ . The  $\mathbf{e}_t$  is a noise or error term with a diagonal or nondiagonal covariance matrix. Granger's equation corresponds to the TS vector autoregressive model being treated as a simple causal model without or with contemporaneous causal effects at  $t = 0$ . Tank et al. [55] present nonlinear Granger methods using structured multilayer perceptrons and recurrent neural networks. They combine sparsity-inducing convex group-lasso penalties on the weights that attempt to extract the Granger causal structure by encouraging specific sets of weights to be zero. The predictability characterization of Granger may not directly imply a causal effect of  $\mathbf{y}$  on  $\mathbf{x}$ , improving the prediction of  $\mathbf{x}$  does not necessarily mean  $\mathbf{y}$  causes  $\mathbf{x}$ . The effectiveness of the Granger method in deducing causal connections has thus been a subject of ongoing discussion because of the assumption that predictability implies causality, sensitivity to temporal aggregation and subsampling, and unmeasured confounder effects [52]. Nonetheless, the Granger method remains a valuable tool for analyzing TS data and is widely utilized across various domains, including economics, finance, genomics, and neuroscience [52].

References [3, 22–25] introduce and extend variants of PCMCI, an extension of the PC algorithm [29] leveraged with false-positive cleaning momentary conditional independence for TS CD. The PCMCI methods with linear and non-linear



conditional independence tests outperform state-of-the-art techniques in causality detection on large TS data sets across a range of research fields [23]. Gerhardus et al. [3] propose Latent-PCMCI that relaxes the causal sufficiency assumption of PC extends PCMCI to enhance recall CD with unknown latent confounders using FCI. Saggioro et al. [25] extend the PCMCI to handle non-stationarity with regime-dependent causal graphs using a time-windowing method. A slightly different approach is adopted in the time-aware PC (TPC); it employs the PC algorithm for TS by considering time delay, bootstrapping, and pruning [53]. The approach proceeds by unrolling the TS data (adding new nodes with time delay tags) and generating DAG by applying a set of conditions: using causality can only apply forward-in-time to direct edges, and weight thresholding to prune the graph when rolling the DAG. The bootstrapping samples time-window data iteratively to fine-tune the DAG.

Deep learning (DL) models have also been explored for GCM on TS data [11]. Nauta et al. [11] present a temporal CD framework (TCDF) using the attention scores of the prediction convolutional network. The TCDF consists of k-independent prediction networks based on the temporal convolutional network, where k is the number of TS. Each network performs CD through the attention mechanism that obtains the causal time delay information through convolutional kernel weight routes. The sequences other than the target TS are fed into the network for the prediction process of a given target. The sequence with a high attention score is the causal sequence of the target sequence. Training prediction models for each variable may constrain the TCDF scalability when the number of variables increases, which is the case in large complex systems.

### 2.3 Bayesian Networks

Once the causal graph structure is identified, the second stage of CD is parameterizing the links. Probabilistic parameterization methods such as Bayesian networks allow flexible and faster querying for causal inference. A *Bayesian network* (BN) is a probabilistic graphical model representing variables and their conditional dependencies through a directed acyclic graph [26]. BNs are parameterized using *conditional probability distributions* (CPD), each node  $n$  in the network is modeled as  $P(n | \mathbf{PA}(n))$  where  $\mathbf{PA}(n)$  represents the parents of a node in the network. Bayesian networks represent causal relationships between the variables using CPDs as measures of the causal strength between nodes. Causality modeling with BNs from a given data involves two phases: 1) building the DAG topology structure, and 2) estimating CPD parameters of the DAG. Although parameter estimation is considered a well-studied subject and can be achieved with less computation cost even with limited data availability, learning the DAG structure is more difficult with exponential computational cost as the data and number of variables grow.

**Definition 2** A Bayesian network is a probabilistic representation of joint distributions over the variables using a DAG model. The CPD is computed using the DAG from data using Bayes and chain rules of probability as follows:

$$P(A, B, C) = P(A|B, C)P(B|C)P(C) \quad (4)$$

The equation shows that the joint distribution of all variables is the sum of all CPDs in the network. Representing the joint distribution's independence in a graph structure allows storing fewer BN parameters. *Maximum likelihood estimation* and *Bayesian parameter estimator* are widely employed BN parameter learning methods [44]. The maximum likelihood estimates the CPDs simply using the relative frequencies with which the variable states have occurred. However, this approach has the problem of overfitting the data; for example, it will be extremely far off for small data that are not fully representative of the underlying distribution. The Bayesian parameter estimator mitigates the overfitting issue of the maximum likelihood estimation by starting with already existing CPDs using prior histogram counts before the data was observed. For instance, the *K2-prior* adds prior initial pseudo-state counts (adds 1) to the actual counts before normalization. Those "priors" are then updated using the state counts from the observed data. Another choice of prior is the *Bayesian Dirichlet equivalent uniform prior* which assumes the Dirichlet prior distribution over the parameters of the network that reflect a uniform distribution over possible values [44].

## 3 Dataset Description

### 3.1 The HCAL Readout Box Monitoring Data set

The CMS HCAL is a specialized calorimeter that captures hadronic particles during a collision event in the CMS experiment (see Figure 2) [56, 57]. The primary purpose of the HCAL is to measure the energy of hadrons by absorbing their energy and converting it into measurable signals. The calorimeter is composed of brass and plastic scintillators, and the scintillation light produced in the plastic is transmitted through wavelength-shifting fibers to *Silicon photomultipliers* (SiPMs) (see Figure 3) [57, 58]. The HCAL front-end electronics consist of components responsible for sensing and digitizing optical signals of the collision particles. The front-end electronics are divided into sectors of

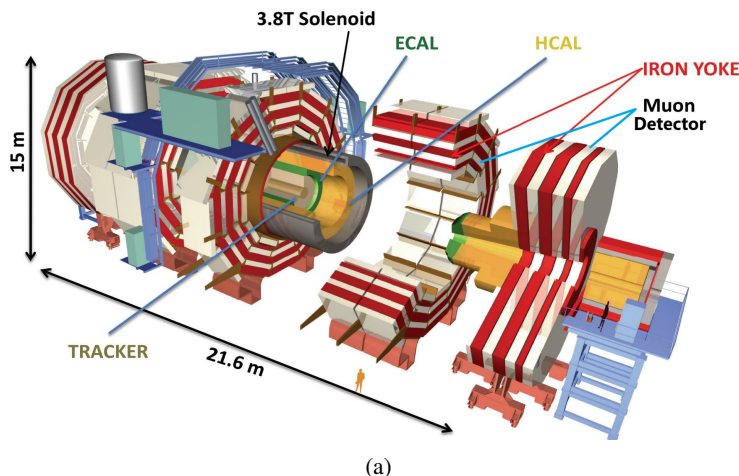


Figure 2: Schematic of the CMS experiment [59].

*readout boxes* (RBXes) that house and provide voltage, backplane communications, and cooling to the data acquisition electronics.

The HCAL is made of four subsystems (subdetectors): the HCAL Endcap (HE), the HCAL Barrel (HB), the HCAL Forward (HF), and the HCAL Outer (HO) [60]. The front-end electronics of the HE, the use-case of our study, is made of 36 RBXes arranged on the plus and minus hemispheres of the CMS detector [60, 61]. Each RBX houses four *readout modules* (RMs) for signal digitization [58]; each RM has a SiPM control card, 48 SiPMs, and four readout cards—each includes 12 *charge integrating and encoding chips* (QIE11) and a *field programmable gate array* (Microsemi Igloo2 FPGA). The QIE integrates charge from each SiPM at 40 MHz, and the FPGA serializes and encodes the data from the QIE. The encoded data is optically transmitted to the backend system through the CERN *versatile twin transmitter* (VTTx) at 4.8 Gbps.

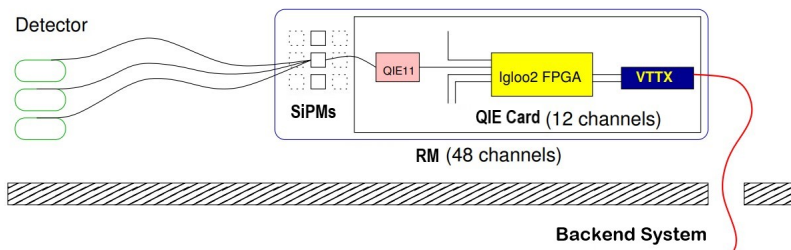


Figure 3: The frontend electronics of the HE data acquisition chain, including the SiPMs, the frontend readout cards, and the optical link connected to the back-end electronics [58]. Each readout card contains twelve QIE11 for charge integration, an Igloo2 FPGA for data serialization and encoding, and a VTTx optical transmitter.

Our HCAL use case dataset includes sensor readings from the RMs of the thirty-six RBXes in the HE detector. Each RM has twelve diagnostic sensors, four from the SiPM control card and eight from four QIE cards (see Table 1). The dataset was obtained from the HCAL online software monitoring system (the ngCCM server) from 01/08/2022 to 30/11/2022. The monitoring sensor data comprises four-month data of 20.7M samples, around 12K per sensor per RM. The dataset contains irregularly sampled and considerably sparse data, a few samples are logged every eight for the SiPM control card and two hours for the QIE card sensors. We utilize data from all four RMs of the RBX-HEP07 at one-minute intervals for the online AD and CD evaluation; the RBX-HEP07 is one of the RBX with diverging behavior [62]. We removed the extended reading gaps due to various non-physics activities on the LHC. We interpolated (up to eight-hour gaps) the remaining time regions into one-minute intervals in data preprocessing. The final dataset contains 100K samples per RM per sensor, 4.8M data samples.

### 3.2 EasyVista Monitoring Public Data set

EasyVista [63] has provided a multivariate sensor dataset from their information technology monitoring system and made the data publicly available in Ref. [64]. The dataset consists of eight TS variables collected with a one-minute

Table 1: HE-RM monitoring sensor data variables description.

No.	Notation	Variable Name	Remark
1	SPV	PELTIER_VOLTAGE_F	Voltage of the SiPM Peltier temperature controller
2	SPC	PELTIER_CURRENT_F	Current of the SiPM Peltier temperature controller
3	SRT	RTDTEMPERATURE_F	SiPM control card temperature averaged over 50 samples
4	SCH	HUMIDITY_F	SiPM control card humidity
5	Q1H	1-B-SHT_RH_F	QIE card 1 humidity
6	Q2H	2-B-SHT_RH_F	QIE card 2 humidity
7	Q3H	3-B-SHT_RH_F	QIE card 3 humidity
8	Q4H	4-B-SHT_RH_F	QIE card 4 humidity
9	Q1T	1-B-SHT_TEMP_F	QIE card 1 temperature
10	Q2T	2-B-SHT_TEMP_F	QIE card 2 temperature
11	Q3T	3-B-SHT_TEMP_F	QIE card 3 temperature
12	Q4T	4-B-SHT_TEMP_F	QIE card 4 temperature

sampling rate (see Table 2). Following Assaad et al. [31], we utilize a data segment, indexed from 45683 to 50000, for our CD evaluation; each of the sensors is considered anomalous with collective anomalies that have the same time of appearance and duration.

Table 2: EasyVista monitoring data variables description.

No.	Notation	Remark
1	PMDB	The extraction of some information about the messages the Storm ingestion system received.
2	MDB	Activity of a process that orients messages to another process with respect to different types of messages.
3	CMB	Activity of extraction of metrics from messages
4	MB	Activity of insertion of data in a database.
5	LMB	Activity of updates of the last metrics values in Cassandra.
6	RTMB	Activity of searching to merge data with information from the check message bolt.
7	GSIB	Activity of insertion of historical status in the database.
8	ESB	Activity of writing data in Elasticsearch.

## 4 Methodology

This section presents our proposed ANOMALYCD approach for anomaly CD on TS data sets.

We present the ANOMALYCD framework for anomaly causality diagnostics that addresses the challenges of CD of binary anomaly data sets. The proposed system comprises two main modules, i.e., causal graph discovery and causality inference (see Figure 4). The causal graph discovery generates temporal causal networks and trains a BN inference model on the input anomaly data streamed from trained (or online) AD systems. The causality inference modules handle user queries with observation conditions and provide causality and conditional probabilities using the BN model. The causality inference queries on the causal graph network include:

- *Conditional probability inference*: Probabilistic inference allows users to query the BN model for any marginal distribution of anomaly occurrence. The inference module provides features to estimate the causal effect between two variables on a given observed anomaly evidence. We employ *variable elimination* algorithm, an exact inference technique for solving Bayes’ equations, to estimate conditional distributions over a subset of variables from the probabilistic graphical BN models.

$$C_i = \wp(\mathcal{B}, x_i, S) \quad (5)$$

where  $C_i$  is the conditional probability of the  $x_i \in \{0, 1\}$  sensor for its anomaly flag state  $s_i = 1$  given the observed evidence on other sensors with states of  $S = \{s_j \in \{0, 1\}, \forall j \neq i\}$ . The  $\wp$  is the inference engine with the BN  $\mathcal{B}$ .

- *Check for causality*: Infers the status of common cause between two sensors with active anomaly flag given evidence of anomaly condition status of the other sensors. It checks if there is an active trail, or *d-connection* between the start and end nodes, given that the evidence is observed.

We have previously trained deep-learning AD models on frontend electronics of the HE detector, including the *next-generation clock and control module* (ngCCM), RM and data quality monitoring (DQM) [13–16]. The HE-ngCCM



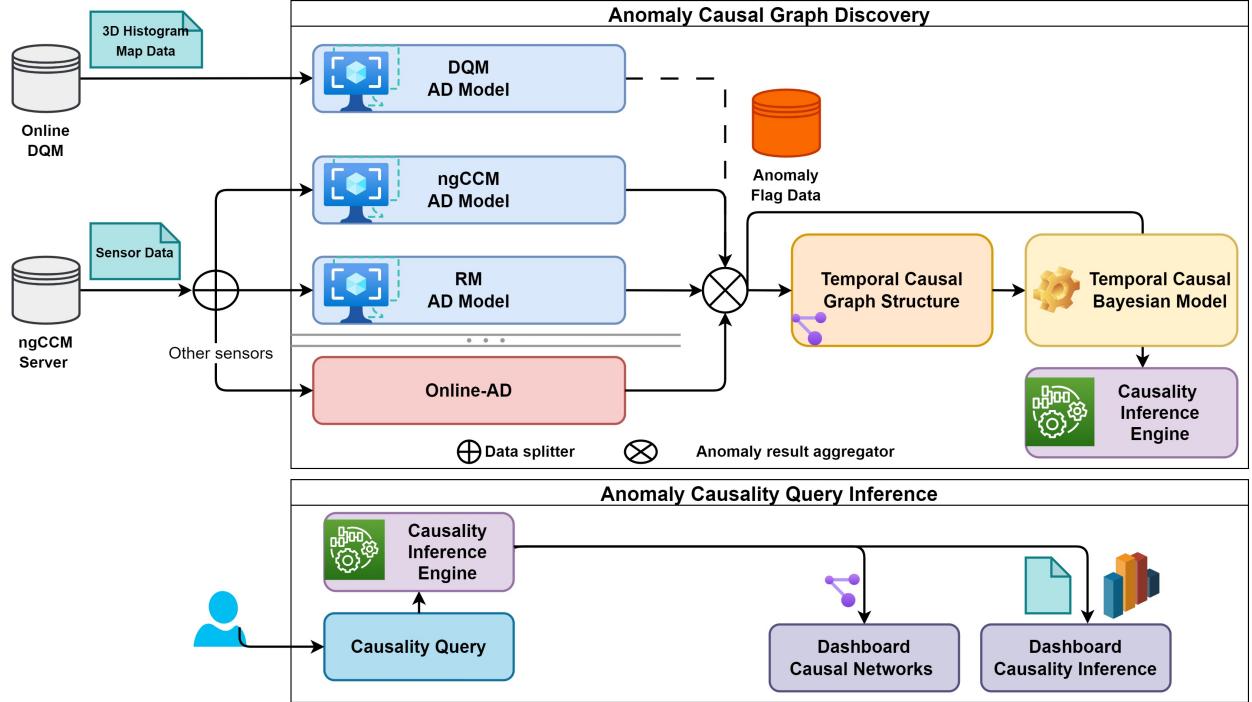


Figure 4: ANOMALYCD: our anomaly CD framework: use-case of the HCAL monitoring. The approach builds a GCM and a BN on the binary anomaly-flag data generated from several systems using trained and online-AD tools.

AD model monitors the HE *clock and control module* of the 36 RBXes, each with 28 sensors [13, 14]. The HE-RM AD model, which adopted Ref. [13], monitors the *readout module* of the RBXes (each RBX has 4 RMs, and each RM has 113 sensors). The DQM-AD monitors 3D spatial data of around 7K physics acquisition channels, 48 channels per RM [15]. The HCAL also comprises several electronic components, and it is often essential to investigate several systems in the pipeline to diagnose and identify root causes of system faults. We incorporate online temporal AD that detects anomalies on variables that are not actively monitored by the previously trained models in Refs. [13–16]. Since we have already discussed the above trained AD models in our previous works [13–16], we will focus below on the proposed online AD and CD approaches.

#### 4.1 Online Time Series Anomaly Detection

We present an online AD algorithm to detect outlier temporal patterns and generate anomaly flags for sensor variables that trained DL models do not actively monitor; we incorporate the algorithm into the proposed CD framework. Different types of variations can occur in TS data, including long-term trends, seasonal changes, periodic fluctuations, and nonrandom sources of variations [65]; these variations can impact the modeling approach and algorithm choices. Building a generic one-fits-all approach is challenging as the requirements depend on signal characteristics and target application. We propose online AD on univariate TS data to capture typical points and collective anomalies, including transient changes in time and frequency, and gradual signal trend drifts. The approach consists of an ensemble of three TS time- and frequency-domain outlier detection algorithms (see Algorithm 1): 1) detecting temporal outliers, 2) detecting changes in temporal trends, and 3) detecting outliers in the spectral domain.

1. *Temporal outlier detection* (see TEMPORALOUTLIERDETECTION in Algorithm 1): The temporal outlier detection employs sliding z-score MOVINGSDOUTLIERDETECTION), and TRENDDRIFTDETECTION on decomposed TS data. We apply *seasonal and trend decomposition* algorithm from Ref. [66] to estimate the trend and residual signals, represented by  $x_t$  and  $x_\epsilon$ , respectively:

$$\begin{aligned}
 x(t) &= x_t(t) + x_\zeta(t) + x_\epsilon(t) \\
 x_t(t) &= (h_p * x)(t), \text{ where } h_p(t) = \frac{1}{p}[1, 1, \dots, 1]
 \end{aligned}
 \tag{6}$$

The additive trend  $x_t$  is obtained by applying a convolution ( $*$ ) filter  $h_p$  with the shape of  $1 \times p$  (a moving average with period  $p$ ) to the data. The average of this de-trended series (after trend removal) for each period

is the returned seasonal component  $x_\zeta$ , and the final remaining component of the series becomes the residual error  $x_\epsilon$ .

The value of  $p$  can be estimated using period estimation methods such as *auto-correlation function*, *fast Fourier transform* (FFT), *periodogram* (based on FFT), *summary statistics subsequence*, and hybrid of method for oscillatory signals [67, 68]. While these methods show good accuracy for cyclic signals with multiplicative trends, we have observed performance deterioration in most methods with additive trends, particularly on signals with higher slopes. We employ FFT on  $\Delta x(t) : x(t) - x(t - 1)$ , in the SIGNALPERIODESTIMATION, to enhance the period estimation accuracy in the presence of additive or multiplicative trends. The employed decomposition method in Eq. (6) assumes an additive trend and single seasonality or cyclic pattern. One may employ multiplicative trend or multi-seasonal component decomposition depending on the expected normal signal characteristics [69].

We utilize a sliding z-score outlier detection algorithm on the detrended residual signal  $x_\epsilon$  (see MOVINGSDOUTLIERDETECTION in Algorithm 1). The  $x_\epsilon$  signal is normalized by subtracting the mean  $\mu_w$  and dividing it by the standard deviation  $\sigma_w$  using a sliding time window ( $w_\theta$ ) to generate the outlier score  $\lambda_\theta$ . The sliding window localizes the outlier detection on the signal characteristics at the adjacent time data points. The  $\mu_w$  and  $\sigma_w$  can be affected by strong outliers in a given data, reducing outlier detection efficacy and gets worse for smaller sliding windows; we utilize thus data quantiles  $Q = [10\%, 90\%]$  along with a median centering instead of mean to reduce the sensitivity to outlier contamination. We apply a threshold on the outlier score to generate the outlier flags  $\Lambda_\theta$ .

We develop a cumulative-based algorithm to detect trend drifts in the trend signal  $x_t$  (see TRENDDRIFTDETECTION in Algorithm 1). We estimate the trend score  $\lambda_t$  using cumulative sum on the first-order difference of the trend  $x_t$  signal, and steps are given in lines 17–25. The trend score resets when more significant signal jumps are detected, often during system configuration changes in the HCAL sensor data; the z-score and spectral methods capture such sudden shifts in the steady state of a signal. We apply threshold  $\alpha_t$  to get the trend drift outlier flags  $\Lambda_t$ .

2. *Spectral outlier detection* (see SPECTRALOUTLIERDETECTION in Algorithm 1): We employ spectral residual (SR) saliency detection to identify frequency spectrum or data rate change outliers. The SR method has been employed as a preprocessing technique for cleaning outliers and transforming data in semi-supervised AD research, as demonstrated in Refs. [13] and [70], respectively. The SR algorithm consists of three major steps for a given univariate sequence  $\mathbf{x}$  [70]: 1) FFT  $\mathfrak{F}$  to get the log amplitude spectrum; 2) calculation of spectral residual; and 3) inverse FFT  $\mathfrak{F}^{-1}$  that transforms the sequence back to the time domain and generate saliency outlier scores:

$$\begin{aligned}
 A(f) &= \text{Amplitude}(\mathfrak{F}(\mathbf{x})) \\
 P(f) &= \text{Phase}(\mathfrak{F}(\mathbf{x})) \\
 L(f) &= \log(A(f)) \\
 L_h(f) &= h_q(f) * L(f) \\
 R(f) &= L(f) - L_h(f) \\
 \eta(\mathbf{x}) &= \|\mathfrak{F}^{-1}(\exp(R(f) + iP(f)))\|
 \end{aligned} \tag{7}$$

where  $\mathbf{x}$  is the input sequence with shape  $1 \times T$ ;  $A(f)$  is the amplitude spectrum;  $P(f)$  is the corresponding phase spectrum;  $L(f)$  is the log representation of  $A(f)$ ; and  $L_h(f)$  is the average spectrum of  $L(f)$  which can be approximated by convoluting with  $h_q(f)$ , where  $h_q(f) = \frac{1}{q}[1, 1, \dots, 1]$  is averaging filter with an  $1 \times q$  vector.  $R(f)$  is the spectral residual, the difference between the log spectrum  $L(f)$  and the averaged log spectrum  $L_h(f)$ . The sequence is transferred back to the time domain via  $\mathfrak{F}^{-1}$  to get the saliency signal  $\eta$ . We apply a threshold  $\alpha_\eta$  to detect anomaly points on  $\eta$  and generate flags,  $\Lambda_\eta$ .

## 4.2 Anomaly Causal Discovery

Graph-based anomaly CD generates an equivalent DAG representing the causal interaction among the monitored variables. Computing a DAG for the temporal CD of anomalies in large systems with multiple variables and large data is challenging. We incorporate several methods to address the data size challenges of CD on the binary anomaly data  $\Lambda$ . The methods include 1) data size compression using sparse handling algorithms, 2) sparsity-driven prior time-delay link assumption compression, 3) one-side edge independence testing for anomaly triggering from flag 0 to 1 transitions, and 4) post-processing link adjustment to avoid cyclic edges on different time-lags. The proposed methods assist in alleviating the computational burden and improving the accuracy of the anomaly CD.

Our proposed anomaly CD framework includes three main modules: data preprocessing, causal graph structure generation, and building the BN inference model. The approach infers the temporal causal graph among monitoring

**Algorithm 1** Online temporal anomaly detection

---

```

1: procedure ONLINETEMPORALANOMALYDETECTION( $\mathbf{x}, p_l, \alpha_\theta, w_\theta, \alpha_l, k_l, \alpha_\eta, q_\eta$ )
  ▷ Ensemble online temporal AD
  ▷  $\mathbf{x}$  is a univariate TS signal data
2:    $\Lambda_\theta, \Lambda_l \leftarrow$  TEMPORALOUTLIERDETECTION( $\mathbf{x}, p_l, \alpha_\theta, w_\theta, \alpha_l, k_l$ )           ▷ detects temporal transient and gradual trend outliers in the time domain
3:    $\Lambda_\eta \leftarrow$  SPECTRALOUTLIERDETECTION( $\mathbf{x}, \alpha_\eta, q_\eta$ )                               ▷ detects spectral outliers in the frequency domain
4:    $\Lambda \leftarrow \Lambda_\theta \cup \Lambda_l \cup \Lambda_\eta$                                                ▷ union of binary outlier flags
  return  $\Lambda$ 
5: procedure TEMPORALOUTLIERDETECTION( $\mathbf{x}, p_l, \alpha_\theta, w_\theta, \alpha_l, k_l$ )
  ▷ Temporal outlier detection
  ▷  $p_l$  is the window size of the convolutional filter for trend estimation
6:   if  $p_l$  is NULL then                                                           ▷ for auto period estimation
7:      $p_l \leftarrow$  SignalPeriodEstimation( $\mathbf{x}$ )                                       ▷ signal period estimation using FFT
8:      $x_l, x_c, x_e \leftarrow$  TimeSeriesDecomposition( $\mathbf{x}, p_l$ )                       ▷ decomposition into a trend, cyclic and residual components
9:      $\Lambda_\theta \leftarrow$  MOVINGSDOUTLIERDETECTION( $x_e, \alpha_\theta, w_\theta$ )
10:     $\Lambda_l \leftarrow$  TRENDDRIFTDETECTION( $x_l, \alpha_l, k_l$ )
  return  $\Lambda_\theta, \Lambda_l$ 
11: procedure MOVINGSDOUTLIERDETECTION( $x_e, \alpha_\theta, w_\theta$ )
  ▷ Residual moving standard deviation temporal outlier detection
  ▷  $\alpha_\theta$  is the detection threshold
  ▷  $w_\theta$  is sliding time-window size
12:    $\lambda_\theta \leftarrow []$ 
13:   for  $\mathbf{x}_w \in$  GetSlicedTimeWindowData( $x_e, w_\theta, \text{step} = 1$ ) : do                 ▷ get of data slice from sliding time-windows
14:      $\mu_w, \sigma_w \leftarrow$  GetStats( $\mathbf{x}_w$ )                                         ▷ sliding window median and standard deviation using quantile  $Q = [10\%, 90\%]$ 
15:      $\lambda_\theta \leftarrow$  Append( $\lambda_\theta, |\mathbf{x} - \mu_w|/\sigma_w$  given  $\sigma_w \neq 0$ )     ▷ outlier score
16:    $\Lambda_\theta \leftarrow \lambda_\theta > \alpha_\theta$                                            ▷ temporal outlier flag
  return  $\Lambda_\theta$ 
17: procedure TRENDDRIFTDETECTION( $x_l, \alpha_l, k_l$ )
  ▷ Cumulative sum-based trend drift outlier detection
  ▷  $\alpha_l$  is the detection threshold
  ▷  $k_l$  is a scaling constant
18:    $d_l \leftarrow \Delta(x_l) : x_l(t) - x_l(t - 1)$                                    ▷ step change of trend data points
19:    $\mu_{d_l} \leftarrow$  MEDIAN( $|d_l|$ )                                                  ▷ average set change on the trend
20:    $\bar{d}_l \leftarrow |d_l| > k_l \mu_{d_l}$                                              ▷ check for large step changes in the trend
21:    $\lambda_l \leftarrow$  ZEROS(SIZE( $x_l$ ))                                             ▷ placeholder for the trend anomaly scores with size of  $x_l$ 
22:   for  $t_r, \bar{d}_{l,r} \in$  GetContinuousRegion( $\bar{d}_l$ ) : do   ▷  $\bar{d}_{l,r} \in \{0, 1\}$  is the value of the uniform region  $r$  and  $t_r$  is the corresponding time stamps of  $r$ 
23:     if  $\bar{d}_{l,r}$  then
24:        $\lambda_l(t_r[j]) \leftarrow \sum_{i=1}^j d_l(t_r[i])$ , for  $j = [1, \dots, N_r]$    ▷ calculates trend drift score using cumulative sum and  $N_r$ , the length of  $r$ 
25:    $\Lambda_l \leftarrow \lambda_l > \alpha_l$                                              ▷ trend outlier flag
  return  $\Lambda_l$ 
26: procedure SPECTRALOUTLIERDETECTION( $\mathbf{x}, \alpha_\eta, q_\eta$ )
  ▷ Spectral residual (SR) temporal outlier saliency detection
  ▷  $\alpha_\eta$  is the detection threshold
  ▷  $q_\eta$  is siding spectral kernel size
27:    $\eta \leftarrow$  SpectralResidualSaliency( $\mathbf{x}, q_\eta$ )                               ▷ spectral residual saliency score
28:    $\lambda_\eta \leftarrow \frac{\eta - \bar{\eta}}{\bar{\eta}}$                                                  ▷ normalized outlier score
29:    $\Lambda_\eta \leftarrow \lambda_\eta > \alpha_\eta$                                            ▷ spectral outlier flag
  return  $\Lambda_\eta$ 

```

---

variables or sensors using time-lagged and contemporaneous CD algorithms (see Figure 5). We employ PCMCI for its accuracy in temporal CD in large data sets [24, 71] and propose additional augmentation algorithms to enhance its effectiveness with particular challenges of binary anomaly data. The PCMCI may result in cyclic links even if the expected causal graph is acyclic due to errors in estimation when dealing with a long sequence of overlapping binary anomaly regions among sensors [31, 72]. Through sparse data and graph edge compression, CI testing sensitive to binary flag transitions, and link pruning, we reduce the computational cost and enhance the accuracy of causal graph building at the data pre- and post-processing stages.

#### 4.2.1 Sparse Data Handling

The computational cost of CD for TS data varies with the numbers of variables  $N$ , data sample sizes  $n$ , and maximum time-lag  $\tau_{\max}$  [22]. The complexity of the CI test,  $X \perp Y | Z$ :  $X$  independent of  $Y$  conditioned on  $Z$ , is one major factor affecting the computational workload in a constraint-based algorithm [22]; for instance, partial correlation CI test scales with a complexity of  $\mathcal{O}(n(N\tau_{\max})^2)$ . Optimizing computational efficiency by reducing  $n \rightarrow n'$  and  $N \rightarrow N'$  for a given  $\tau_{\max}$  is advantageous. The speed gain also allows the exploration of longer  $\tau_{\max}$  for extended causality search on  $n'$  for the given computation cost on  $n$ . We propose to lessen the computation by reducing the sample data size of  $\Lambda$ , exploiting the anomaly data sparsity. Data sparsity is inevitable in binary anomaly data since anomalies occur rarely and may persist for some time. Our module incorporates sparse data handling that compresses the long-time regions with uniform anomaly status. Hence, anomaly CD can better be captured from the status transitions with much

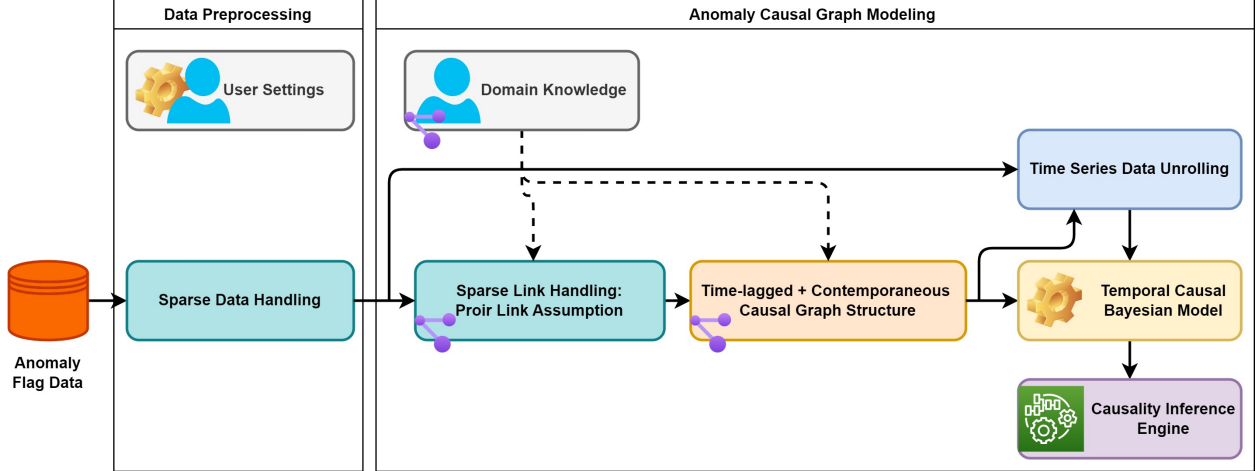


Figure 5: Temporal anomaly CD approach diagram. The approach infers causal interaction among monitoring sensor variables from binary anomaly data.

lower computation on the compressed flag data  $\Lambda_c$  (see Algorithm 2). We preserve the first  $l_m$  indices of the regions to capture the time-lag causality that ensures inference within time-adjacent anomaly occurrences while substantially reducing the size of the remaining sparse uniform regions. We set the time length  $l_m$  slightly greater than the causality searching  $\tau_{\max}$  to avoid false adjacency between anomalies at different time stamps after compression. The  $l_m$  also regulates the contribution between collective trend drift anomalies and transient anomalies; longer  $l_m$  increases the influence of the collective anomalies on the causality estimation and vice-versa. Our method aims to reduce the sample size to partially resolve the computational burden in the GCM learning process for large-scale deployment.

#### 4.2.2 Causal Graph Network Generation

We build a causal graph network generation method for binary anomaly data; we leverage the PCMCI algorithm [3, 24] to learn the graph skeleton  $\mathcal{G}(\mathcal{V}, \mathcal{E})$  from a TS data, where  $\mathcal{V}$  is the set of sensor node vertices  $v, \nu \in \mathcal{V}$ , and  $\mathcal{E}$  is the edge matrix  $\mathcal{E} \subseteq \mathcal{V} \times \mathcal{V} : \varepsilon(v, \nu) \in \mathcal{E}$ . We limit the discussion to our algorithms and leave readers to refer to Refs. [3, 23, 24] for a comprehensive explanation of the working principle of the PCMCI algorithm. Our modification revolves around customization for handling binary anomaly data, reducing computation by prior link assumption, and removing cyclic links from causality confusion in long overlapped anomaly regions.

Constraint-based graph CD methods rely on CI tests to estimate links among variables. The independence score function  $\mathcal{I}(X, Y)$  answers CI queries of the form  $X \perp Y \mid Z$  on given dataset  $\mathcal{D}$  that the variables assumed to be generated independently from some (unknown) Bayesian system as:

$$\mathcal{I}(X, Y) : P(X, Y \mid Z) = P(X \mid Z)P(Y \mid Z) \quad (8)$$

The independence test may result in Type I errors (false positive that rejects true independence) and Type II errors (false negative that accepts false independence), as  $P$  (derived from  $\mathcal{D}$ ) is an approximate description of the actual underlying system behavior. The trade-off of controlling the error is obtained by a significance level threshold  $\alpha$  given independence measuring function  $f_I(\mathcal{D})$ . The  $p_v$ , probability of observing independence of the test, is given as:

$$p_v(\alpha) = f_I(\mathcal{D}) > \alpha \quad (9)$$

We aim to capture the causality linkages behind binary anomaly data, particularly the transition from being healthy with flag 0 to experiencing an anomaly with flag 1. The popular CI tests for categorical data, such as statistical *G-squared* [73] and information-theory *conditional mutual information* tests [3], may not easily distinguish the significance of the anomaly transition behavior; these methods could result in incorrect causality inferred from the association influenced by the zeros instead of the ones. We propose *anomaly-flag aware CI test* (ANAC) using a partial-correlation CI test that only considers links with positive associations corresponding to anomaly occurrence. The PCMCI estimates GCM of a given TS variable (anomaly flag  $\Lambda_i$  in our case) with a time-lagged function of the multivariate:

$$\Lambda_i = \mathcal{F}(w_j(t-s), \Lambda_j(t-s)), \text{ for } s = 0, \dots, \tau_{\max} \text{ and } j \in \mathbf{PA}_i \quad (10)$$

where the  $\Lambda$  is the multivariate anomaly data; the  $w$  is the time-lagged causal weights; the  $\tau_{\max}$  is the maximum time-lag for causal inference; the  $\mathbf{PA}_i$  is the set of the parent nodes or variables of  $i$ ; the  $\mathcal{F}$  is a binary GCM function. The CI test

influences the  $w$ : the positive  $w$  indicates a positive correlation in  $\Lambda_i$ , increasing together during anomaly occurrence. We leverage the PCMCI [24] with ANAC to detect anomaly occurrence causality by selecting causal time-lags with  $w > 0$ . The partial correlation is estimated through *linear ordinary least squares regression* and positive *Pearson’s correlation* ( $\rho$ ) CI test on the residuals. To test  $X \perp Y \mid Z$ , first  $Z$  is regressed out from  $X$  and  $Y$  using the regression model:

$$\begin{aligned} X &= \beta_X Z + \epsilon_X \\ Y &= \beta_Y Z + \epsilon_Y \end{aligned} \tag{11}$$

The independence of the residuals is evaluated using Student’s t-test on the  $\rho(\epsilon_X, \epsilon_Y)$  to generate the  $p_v$ .

The CD may remain complex for high-dimensional data with large  $N$  despite the partial reduction of the computation by sparse data compression [24]. Hence, we incorporate a sparse link handling algorithm that assumes prior links to reduce the link searching space. The method aims to relieve the computation by reducing the number of conditional tests. The prior link assumption excludes self-lag causality and non-overlapping links on the binary anomaly data that  $\mathbf{PA}_i \in X_j(t-s), \forall j \neq i$ . The assumption of self-lag exclusion reduces the computation of the link search from  $\mathcal{O}(n'(N\tau_{\max})^2)$  to  $\mathcal{O}(n'(N-1)N\tau_{\max}^2)$ . The non-overlapping links assumption excludes prior links from temporally non-overlapping signals and eases the computation further to  $\mathcal{O}(n' \sum_i^N N'_i \tau_{\max}^2)$ , where,  $N'_i \leq N-1$ ) (see Algorithm 3). The algorithm extends the anomaly flag regions by  $\tau_{\max}$  to calculate the overlap score that measures the time-lagged co-occurrence among a pair of variables, and a link is not considered during the learning phase if the overlap score is below a certain threshold, e.g., zero indicates no overlap.

### 4.2.3 Causal Edge Pruning and Adjustment

Multiple sensor variables can report anomaly flags simultaneously for continuous time ranges that might cause the PCMCI [3, 24] to generate PDAG, which includes spurious edges—multiple time-lags, undirected, or cyclic links—when dealing with a temporal anomaly data. Bidirected edges also occur when there is no time delay causality; the correlation-based CI tests are symmetric and cannot distinguish the edge direction at  $t = 0$ . We present a pruning algorithm as post-processing to overcome this challenge (see Algorithm 4). The algorithm groups linked nodes and keeps the lag with the highest weight or earliest time-lag from the reported causal lags; higher link weights indicate stronger causality, and older time-lags correspond to earlier causality that is temporally close to the transitioning edges. We employ a chi-square test to direct the bidirected edges at  $t = 0$  when the correlation CI test falls short in detecting the directions. The positive transition association of the anomaly flags on the directed edges holds even in the chi-square test since the edges are first detected using positive correlation scores. The pruning excludes the spurious links caused by the continuously overlapped regions and enables the correlation test to generate a curated DAG that meets the requirement for building the inference BN model for causality query in the later stages, i.e., BN requires a GCM without cyclic links.

## 4.3 Building Bayesian Network Model

We employ a BN to qualify and enable causality inference for user query conditions beyond having a static graph skeleton. We utilize a *Bayesian parameter estimator* [44] using a *Bayesian Dirichlet equivalent uniform prior scoring* to learn the Bayesian CPD parameters of the discovered network skeleton structure of the PCMCI temporal GCM. The edges of the generated temporal causal graph  $\mathcal{G}((v, \nu), \varepsilon(w, s))$  have weight  $w$  and time-lag  $s$  attributes. To build a temporal causal BN, we reformulate  $\hat{\mathcal{G}}(\mathcal{V}, \mathcal{E}) : (v, \nu) \rightarrow (v_s, \nu), \varepsilon(w, s) \rightarrow \varepsilon(w_s)$  that source node  $v$  with an edge  $\varepsilon(w, s)$  is represented by new nodes  $v_s$  and an edge  $\varepsilon(w_s)$  for every active time-lag  $s$ . We prepare the data for the  $v_s$  by unrolling the TS data of the  $v(t)$  into structural data, a new column with  $v_s$  is added by shifting the data ahead by the amount of time-lag  $s$  (see Algorithm 5, similar unrolling approach was adopted in TPC [53] for TS CD using PC). There are also other tools to build TS BN, such as dynamic BNs, but most are restricted to 2-time step temporal BN that requires only unit time-lag links or existence of self-lag connections [74, 75].

## 5 Results and Discussion

### 5.1 Experiment Results on the HCAL Anomaly Data

We discuss the performance of the proposed time-series anomaly CD and analysis framework using a use cause system RBX-HEP07, one of the RBXes that exhibit divergent behavior in the multivariate interconnection analysis in Ref. [62]. We employ the anomaly flags, generated from our proposed online AD algorithm, for the CD experiment.

The dataset comprises 12 sensors of each RM system. Several extended reading gaps exist due to various non-physics activities on the LHC. We generated a reading mask, shown in Figure 6, to filter out the irrelevant operational time



**Algorithm 2** Data compression on sparse binary anomaly flag

```

1: procedure SPARSEBINARYDATAHANDLER( $\Lambda, l_m$ )
    $\triangleright \Lambda \in \mathbb{R}^{N \times T}$  is a matrix of anomaly flags with  $N$  sensors and  $T$  time length
    $\triangleright l_m$  is the maximum time length for uniform states data compression
2:    $\Lambda_c \leftarrow []$   $\triangleright$  the compressed anomaly flags data  $\Lambda_c \in \mathbb{R}^{N \times T_c}$ 
3:    $S \leftarrow \text{AggregateAnomalyState}(\Lambda)$   $\triangleright$  returns sequence of binary concatenation of from all variables
4:   for  $I, l_s \in \text{GetUniformStateTimeRegions}(S)$  : do
    $\triangleright I$  holds indices of the uniform status region with a time length of  $l_s$ 
5:      $\Lambda_I \leftarrow \Lambda[I]$   $\triangleright \Lambda_I$  is the selected uniform status flag region
6:     if  $l_s > l_m$  then
7:        $I_d \leftarrow \text{GetRangeToRemove}(\Lambda_I, l_m)$   $\triangleright$  the tail indices of the region, excluding the first  $l_m$  data points
8:        $\Lambda_I \leftarrow \text{CompressBinayData}(\Lambda_I, I_d)$   $\triangleright$  compressing time length of  $\Lambda_I$  by removing  $I_d$  data indices
9:      $\Lambda_c \leftarrow \text{Append}(\Lambda_c, \Lambda_I)$ 
   return  $\Lambda_c$ 

```

**Algorithm 3** Sparse link handling with refined prior link assumption

```

1: procedure SPARSELINKHANDLER( $\Lambda, \mathcal{E}, \tau_{\max}, \alpha_\tau$ )
    $\triangleright \Lambda$  is multivariate TS data, containing binary anomaly data
    $\triangleright \mathcal{E}$  is a prior assumption of directed time-lagged edge links
    $\triangleright \tau_{\max}$  is the causality search maximum time-lag
    $\triangleright \alpha_\tau$  is time-lagged anomaly flag overlap strength threshold
2:    $d\Lambda \leftarrow \Delta\Lambda : \Lambda(t) - \Lambda(t-1)$ 
3:    $S_{d\Lambda} \leftarrow \text{TimeExtendAnomalyRegion}(size = \tau_{\max})$   $\triangleright$  rolling sum over sliding window of  $window\_size = \tau_{\max}$  and  $step = 1$ 
4:    $\Lambda_\tau \leftarrow S_{d\Lambda} > 0$   $\triangleright$  convert to binary
5:   for  $\Lambda_\tau(i), \Lambda_\tau(j) \in \text{GetUniquePairVariables}(\Lambda_\tau)$  : do
6:      $\lambda_\tau \leftarrow \text{SimultaneousAnomalyFlagCount}(\Lambda_\tau(i), \Lambda_\tau(j))$ 
7:     if  $\lambda_\tau > 0$  then  $\triangleright$  check if overlap exists
8:        $n^i \leftarrow \text{AnomalyFlagCount}(\Lambda_\tau(i))$ 
9:        $n^j \leftarrow \text{AnomalyFlagCount}(\Lambda_\tau(j))$ 
10:       $\lambda_\tau^{ij} \leftarrow \frac{\lambda_\tau}{n^i}$   $\triangleright$  normalized overlap score from  $i$  to  $j$ 
11:       $\lambda_\tau^{ji} \leftarrow \frac{\lambda_\tau}{n^j}$   $\triangleright$  normalized overlap score from  $j$  to  $i$ 
12:      if  $\lambda_\tau^{ij} < \alpha_\tau$  then
13:         $\mathcal{E} \leftarrow \text{RemoveEdges}(\mathcal{E}, i, j)$   $\triangleright$  remove all edges from node  $i$  to  $j$ 
14:      else if  $\lambda_\tau^{ji} < \alpha_\tau$  then
15:         $\mathcal{E} \leftarrow \text{RemoveEdges}(\mathcal{E}, j, i)$   $\triangleright$  remove all edges from node  $j$  to  $i$ 
16:      else
17:         $\mathcal{E} \leftarrow \text{RemoveEdges}(\mathcal{E}, i, j)$   $\triangleright$  remove all edges from node  $i$  to  $j$ 
18:         $\mathcal{E} \leftarrow \text{RemoveEdges}(\mathcal{E}, j, i)$   $\triangleright$  remove all edges from node  $j$  to  $i$ 
   return  $\mathcal{E}$ 

```

regions of the LHC and ensure any detected anomalies are within the normal operation of the calorimeter. We interpolate, up to eight-hour gaps, the remaining regions into one-minute intervals. We utilize data from all RM sensors of the RBX-HEP07 system (RM-1, RM-2, RM-3, and RM-4) to discuss the performance of the proposed methods (see Figure 7). The data comprise short-living transient and time-persistent anomalies, such as trend drifts. We employ data from multiple RMs to capture the global causality of the RM of the HE. We will first discuss the performance of the online AD approach and then proceed to the anomaly CD.

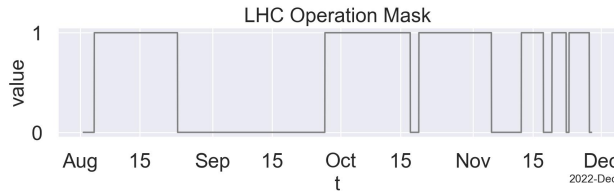


Figure 6: The active mask of the LHC operation status from August to December of 2022. The active  $mask = 1$  refers to the LHC during its normal operation run of collision experiment or idle, whereas the  $mask = 0$  corresponds to the LHC under other non-physics operation states, e.g., technical stop and maintenance development.

**5.1.1 Online Anomaly Detection**

We provide the hyperparameter settings of the online algorithms incorporated in our ensemble AD approach in Table 3. We set the anomaly thresholds slightly higher to reduce noise contamination and preserve the causal faithfulness assumption [6, 29, 49].

**Algorithm 4** Pruning and adjusting time-lagged causality edges

```

1: procedure ADJUSTTEMPORALCAUSALITYLINKS( $\mathcal{E}$ ,  $mOptions = ['edge\_weight', 'edge\_tlag']$ )
   ▷  $\mathcal{E} \in \mathbb{R}^{N \times 4}$  is a matrix of weighted directed time-lagged edge links  $\varepsilon(v, \nu, w, t)$ 
2:    $\mathbf{G}_\varepsilon \leftarrow EdgeGroupMaxWeightedTimeLag(\mathcal{E})$            ▷ groups edges with the same nodes and selects the strongest time-lag
3:    $\mathbf{R} \leftarrow []$                                        ▷ placeholder for edges to be removed
4:    $\mathbf{D} \leftarrow []$                                        ▷ placeholder for undirected edges
5:   for  $\varepsilon_s, \varepsilon_r \in GetBidirectLinkedNodes(\mathbf{G}_\varepsilon)$  : do           ▷ the current edge  $\varepsilon_s$  and the reverse edge  $\varepsilon_r$ 
6:      $\varepsilon_p \leftarrow COMPAREBIDIRECTLINKS(\varepsilon_s, \varepsilon_r, m = mOptions[0])$ 
7:     if  $\varepsilon_p$  is not Edge then
8:        $\varepsilon_p \leftarrow COMPAREBIDIRECTLINKS(\varepsilon_s, \varepsilon_r, m = mOptions[1])$ 
9:     if  $\varepsilon_p$  is not Edge then
10:       $\mathbf{D} \leftarrow Append(\mathbf{D}, [\varepsilon_s, \varepsilon_r])$            ▷ add the edges  $\varepsilon_s$  and  $\varepsilon_r$  into the undirected bucket
11:       $\mathbf{R} \leftarrow Append(\mathbf{R}, [\varepsilon_s, \varepsilon_r])$            ▷ add the edge  $\varepsilon_s$  and  $\varepsilon_r$  into remove bucket
12:    else
13:       $\mathbf{R} \leftarrow Append(\mathbf{R}, \varepsilon_p)$                  ▷ add the edge  $\varepsilon_p$  into remove bucket
14:    else
15:       $\mathbf{R} \leftarrow Append(\mathbf{R}, \varepsilon_p)$                  ▷ add the edge  $\varepsilon_p$  into remove bucket
16:     $\mathcal{E}_R \leftarrow PruneEdges(\mathbf{G}_\varepsilon, \mathbf{R})$                  ▷ remove edges in the remove bucket
17:     $\mathcal{E}_D \leftarrow DirectEdges(\mathbf{G}_\varepsilon, \mathbf{D})$            ▷ get DAG for the undirected edges without affecting the directed edges in  $\mathbf{G}_\varepsilon$ 
18:     $\mathcal{E} \leftarrow Merge(\mathcal{E}_R, \mathcal{E}_D)$                    ▷ merge pruned and directed edges
  return  $\mathcal{E}$ 
19: procedure COMPAREBIDIRECTLINKS( $\mathbf{G}_\varepsilon, \varepsilon_s, \varepsilon_r, m$ )
20:    $t_s, w_s \leftarrow GetEdgeAttributes(\varepsilon_s)$            ▷ get edge link time-lag and weight of link  $s$ 
21:    $t_r, w_r \leftarrow GetEdgeAttributes(\varepsilon_r)$            ▷ get edge link time-lag and weight of the reverse link  $r$ 
22:    $\varepsilon_p \leftarrow None$                                ▷ placeholder for the edge to be pruned
23:   if  $mis'edge\_weight'$  then                             ▷ use link weight values
24:     if  $w_s > w_r$  then
25:        $\varepsilon_p \leftarrow \varepsilon_r$ 
26:     else if  $w_s < w_r$  then
27:        $\varepsilon_p \leftarrow \varepsilon_s$ 
28:   else if  $mis'edge\_tlag'$  then                             ▷ link time-lag values (negative)
29:     if  $t_s < t_r$  then
30:        $\varepsilon_p \leftarrow \varepsilon_r$ 
31:     else if  $t_s > t_r$  then
32:        $\varepsilon_p \leftarrow \varepsilon_s$ 
  return  $\varepsilon_p$ 

```

**Algorithm 5** Temporal Bayesian network model generation

```

1: procedure BAYESIANNETWORKMODELGENERATION( $X, \mathcal{G}$ )
   ▷  $\mathbf{X} \in \mathbb{R}^{N \times T}$  is a multivariate TS data
   ▷  $\mathcal{G}$  is a graph network with  $\mathcal{G}(v, \nu, \varepsilon(w, t))$ 
2:    $\hat{\mathcal{G}} \leftarrow UnrollTemporalGraph(\mathcal{G})$                  ▷ Update node names with edge time-lag value
   ▷ The loop below is for TS data unrolling adopted from TPC [53]
3:   for  $\varepsilon(v_t, \nu) \in GetLinkedNodes(\hat{\mathcal{G}})$  : do
4:      $t \leftarrow GetEdgeTimeLag(v_t)$                    ▷ get source node time-lag
5:     if  $t < 0$  then                                     ▷ checks the time delayed causality
6:        $\hat{x}_v \leftarrow GetTimeDelayedData(x_v, t)$        ▷ shifts backward the TS  $x_v \in \mathbb{R}^{1 \times T}$  by  $t$  time steps
7:        $X \leftarrow Append(\hat{x}_v)$ 
8:    $B \leftarrow FitBayesianNetwork(X, \hat{\mathcal{G}})$              ▷ build BN model
  return  $B$ 

```

The LHC has undergone operations that result in distinct signal patterns on the sensors; we have further utilized change point breaks (on 2022-09-27, 2022-10-19, and 2022-11-12) in which the AD system reinitializes. Change point detection algorithms, such as PELT [76] and kernel-based [77], can detect changes in operation automatically from TS signal data; we found their accuracy is sensitive to hyperparameters and unsatisfactory as false detection increases for non-periodic and non-stationary signals.

Table 3: Hyperparameter settings for the outlier detection algorithms.

Algorithm	Settings (at 1 minute sampling interval)
MOVINGSDOUTLIERDETECTION	$\alpha_\theta = 10, w_\theta = 5760$
TRENDDRIFTDETECTION	$\alpha_\tau = 20, p_\tau = 5760, k_\tau = 5$
SPECTRALOUTLIERDETECTION	$\alpha_\eta = 35, q_\eta = 1440$

Figure 8 depicts the SCH sensors of the four RMs of HEP07 along with the detected transient and trend outliers marked on the outlier score signals of the outlier detection algorithm. The sensors show a drifting trend where they gradually deviate away, dropping or increasing, from its expected optimal values. Figure 9 illustrates all the sensors from RM-1 with marked anomalies. Figure 10 portrays the anomaly flag count from all RMs of the HEP07; the humidity sensors

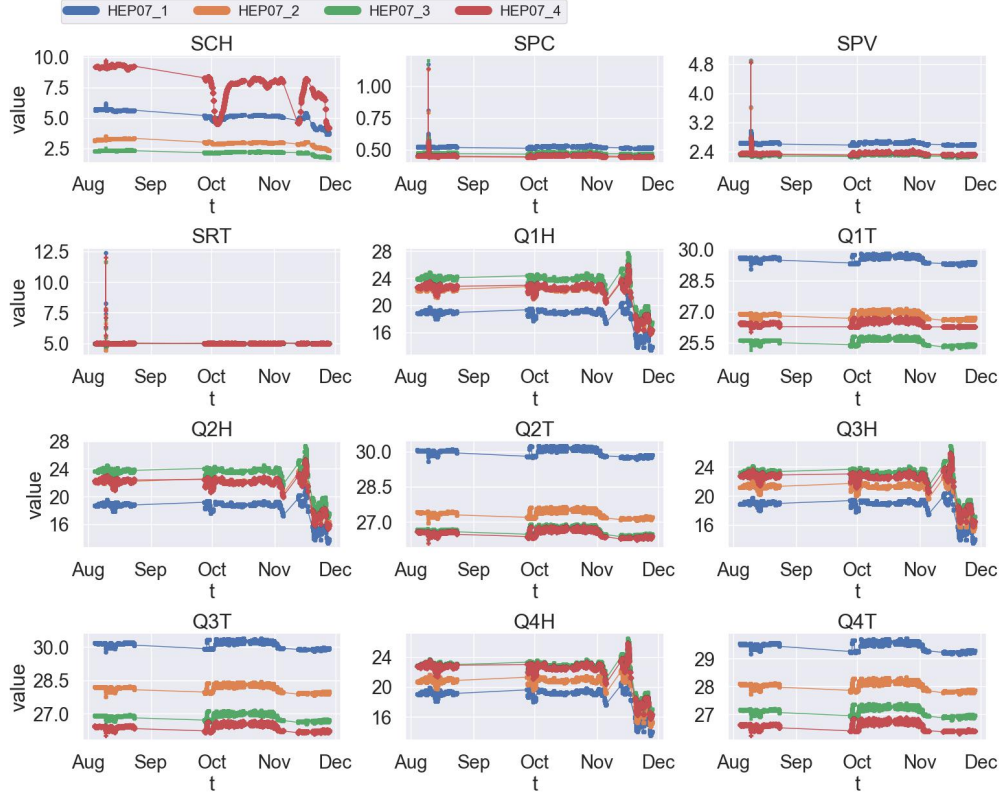


Figure 7: Sensor TS reading data from all four RMs of the RBX-HEP07. The HEP07\_i denotes the  $i^{\text{th}}$  RM of the RBX.

have higher counts due to the detected trend drift anomaly. The time of occurrence of anomalies on the SRT seems temporally correlated with the Q[1-4]T, SPV, and SPC.

We have demonstrated the capability of our proposed online AD approach in detecting several types of outliers on TS data with light computation overhead. The potential limitation of the approach is that it expects adequate healthy data samples, as it is challenging to detect outliers without prior knowledge if the outlier is dominant in data that violates the rare anomaly occurrence assumption. In such cases, using trained AD models is recommended instead. Finding the optimal hyperparameters is also still an open challenge. Data normalization and standardization partially alleviate this challenge, but the hyperparameters may remain dependent on the data or the target outlier characteristics which may require domain knowledge for tuning. Some initial parameter-tuning effort is required when employing the approach in a new environment. Hyperparameter setting adjustment, experimenting with statistical models, is a rather fast process compared to hyperparameter tuning on DL models.

### 5.1.2 Anomaly Graph Causal Discovery and Inference

We capture the causal graph from the TS binary anomaly data generated by the online AD algorithm in the previous section (see Figure 11). We set the maximum time-lag  $\tau_{\max} = 5$  to search for temporal causality dependency at  $t - \tau_{\max}, \dots, t - 1, t$  (equivalent to five minutes) and CI test significance threshold  $p_v = 0.05$  for the PCMC algorithm.

We compute *structural hamming distance* (SHD) and *area under the precision-recall curve* (APRC) to measure the discovered causal DAG quantitatively. SHD is a standard distance metric that compares acyclic graphs based on the counts of the edges that do not match [43, 78]. It computes the difference between the two binary adjacency matrices so that missing or false edges are counted as mistakes. SHD counts two errors for a directed link with the reversed edge: for falsely directing the edge and for missing the correct edge.

$$SHD(\mathcal{G}, \mathcal{H}) \leftarrow \mathcal{N}(i, j) \in V \mid \mathcal{G}(\text{edge}(i, j)) \neq \mathcal{H}(\text{edge}(i, j)) \quad (12)$$

where  $V$  is the set of vertices or nodes of the  $\mathcal{G}$  and  $\mathcal{H}$  graphs, and  $\mathcal{N}$  is the number of mismatched nodes between the  $\mathcal{G}$  and  $\mathcal{H}$ . APRC is a classification metric that evaluates predictions with a confidence score of the area under the curve

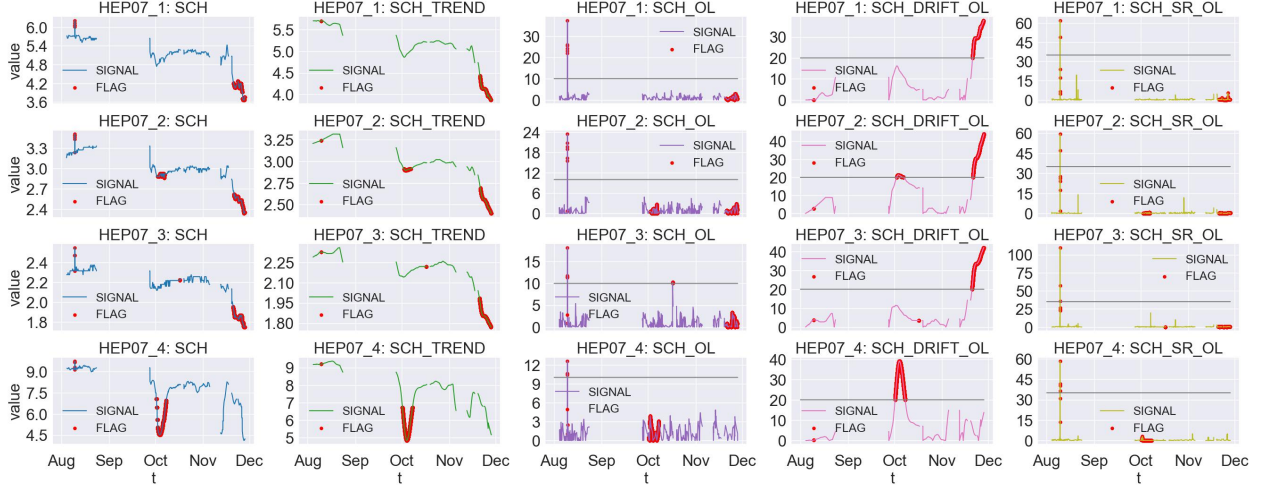


Figure 8: Online temporal AD on RBX-HEP07 SCH sensors. (Left to right) sensor signal, signal trend estimation,  $\Lambda_t$  of TRENDDRIFTDETECTION,  $\Lambda_\theta$  of MOVINGSDOUTLIERDETECTION, and  $\Lambda_\eta$  of SPECTRALOUTLIERDETECTION.

of the *precision* ( $P$ ) and *recall* ( $R$ ) coordinates; the  $P$  and  $R$  are defined as:

$$P = \frac{TP}{TP + FP}, \text{ and } R = \frac{TP}{TP + FN} \quad (13)$$

where  $TP$ ,  $FP$ , and  $FN$  are true positive, false positive, and false negative, respectively:  $TP$  is the number of edges estimated with a correct direction;  $TN$  is the number of edges that are neither in the estimated graph nor in the true graph;  $FP$  is the number of edges that are in the estimated graph but not in the true graph;  $FN$  is the number of edges that are not in the estimated graph but in the true graph.

The sparse data handler, compressing long uniform regions of sparse binary data without anomaly status change across sensors, reduces the data by 99.76% from around  $400K$  to 900 samples. This greatly alleviates the computational cost of the causal graph learning PCMCI algorithm [22, 24]. The compression takes roughly 8 seconds, and it squeezes the uniform regions to  $l_m = 10$  samples, i.e., twice the  $\tau_{\max} = 5$  of the CD (see Figure 11b).

Figure 12 illustrates the temporal GCM structure on the time-lag of  $t = 0, \dots, \tau_{\max}$ , captured by our ANOMALYCD method before link-pruning. The GCM shows expected interconnection among the sensors: the clustering of environmental temperature and humidity sensors, and the link between temperature regulator Peltier voltage and current and the corresponding temperature sensors. Several bi-directed edges with multiple time-lags are also present in the network. Figure 13 shows the final temporal DAG after applying Algorithm 4 for the pruning. An interesting time-lagged causality link can be observed, where a temperature anomaly in SRT leads to anomalies in SPV and SPC; this is because the Peltier regulator responds by increasing SPV and SPC to the upsurge on the SRT.

We have also evaluated the performance of causal structure learning while varying the sparse data compression length  $l_m$ . We have compared the graph accuracy and learning computational time at  $l_m = 10$  with those at  $l_m \in \{15, 20, 25, 30\}$  before and after pruning is applied (see Table 4). We conducted our experiment on a Windows 10 system with an Intel i5-8265U CPU @ 1.60 GHz (8 CPUs) and 16 GB RAM. The PDAGs from the PCMCI algorithm, with spurious links at multiple time lags, lead to higher mismatches among the PDAGs, resulting in lower APRC and higher SHD. The graph matching has improved when we compare the DAGs with pruned links. The closeness of the captured graphs also demonstrates the effectiveness of causality learning on binary anomaly data using the sparse handling algorithm.

We trained our BN model, the query engine for temporal causal inference shown in Figure 5, using unrolled TS data and the captured anomaly DAG skeleton. Table 5 presents the probabilistic anomaly causality inference results using the trained BN. We quantify causality by calculating the anomaly conditional probability (CP) of the causes or affected sensors. The CP of anomaly occurrence for the Q1T sensor increases from 0.05 with no other evidence to above 0.90 with the evidence of a detected anomaly flag on the related Q[2-4]T sensors at a time-lag  $t = 0$ . The CP of an anomaly on the Q1H sensor increases from 0.26 to above 0.85 when there is evidence of a detected anomaly flag on the Q[2-4]H sensors at a time-lag of  $t = 0$ . The Q1H has a higher CP with no other evidence scenario due to trend drifts. We notice the few sample differences during drift detection across the Q[1-4]H sensors lower the causality dependency strength. The CP of SPC increases to 0.45 when SPV has an anomaly at  $t = 0$ . The SRT is causal to the SPC at a time-lag  $t = -1$  directly and at  $t = -5$  through SPV, but with uneven strength of 0.32 and 0.15, respectively. The CP rises to



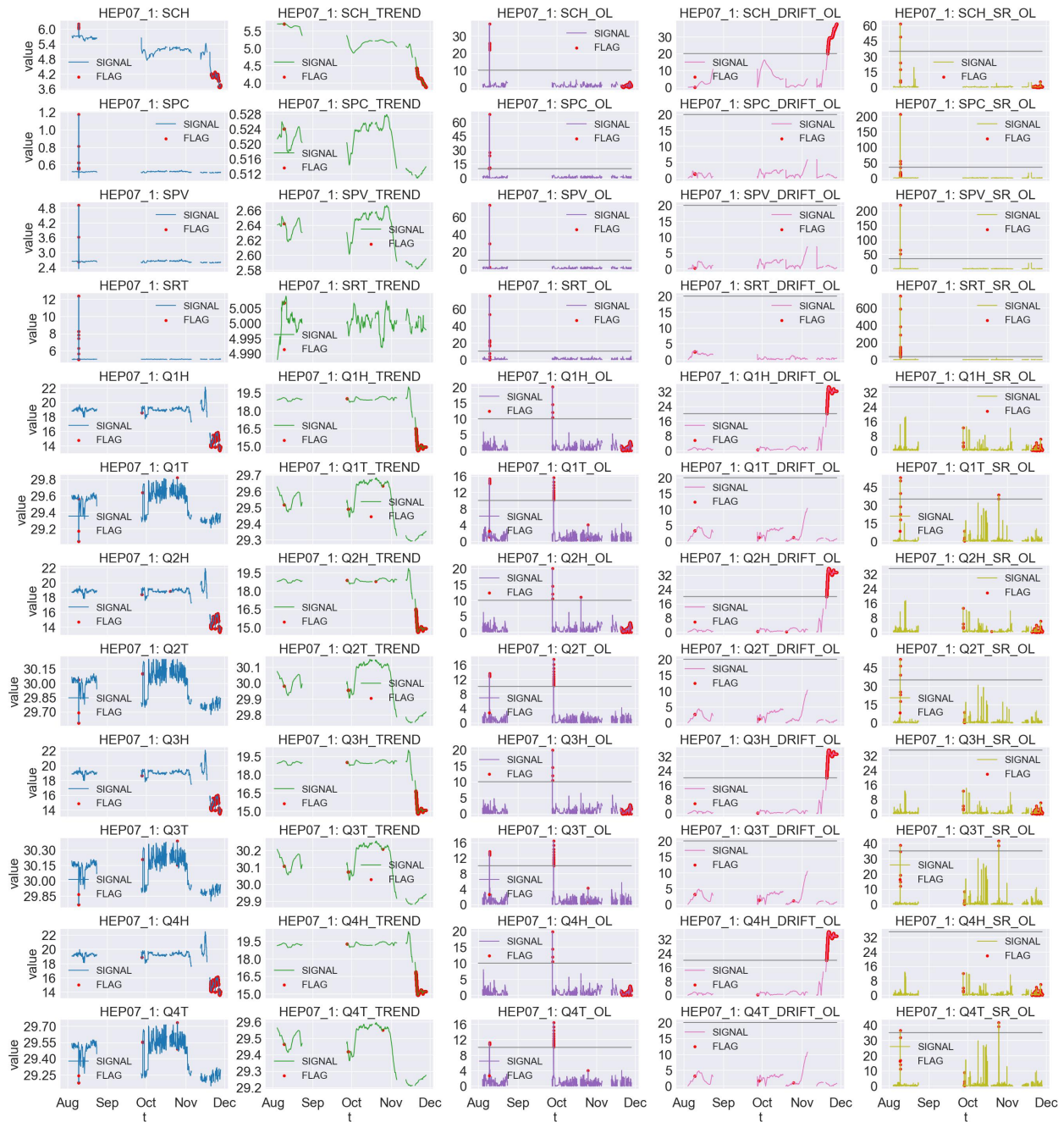


Figure 9: Online temporal AD on the RBX-HEP07-RM-1 sensors.

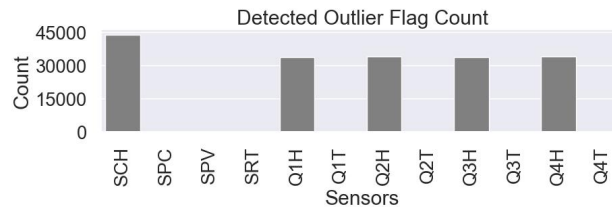


Figure 10: Number of detected anomaly flags from all RMs of RBX-HEP07. The humidity sensors have a higher count due to drifting trends.



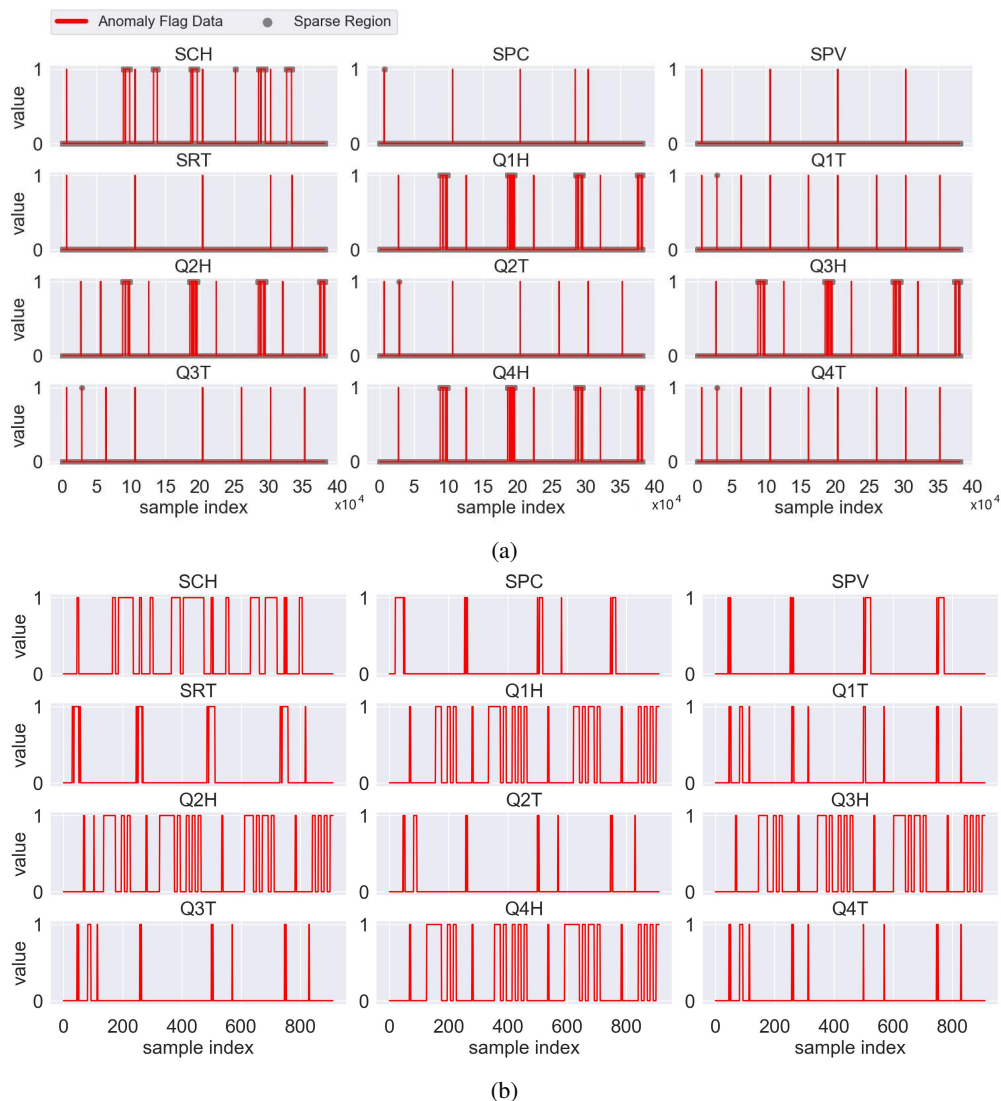


Figure 11: Anomaly binary flag data from our proposed online AD approach on RBX-HEP07 sensors: a) the raw anomaly data with approximately 400K samples and the sparse regions are annotated, and b) sparse compressed data through our sparse handling algorithm with  $l_m = 10$  and reducing the sample size to approximately 900.

Table 4: Causal graph learning comparison on different sparsity length  $l_m$ . The  $SC_t$  is the computation time of the PCMCi skeleton structure learning.

$l_m$	Compressed Data Size	$SC_t$ (sec)↓	Link Pruning Adjustment	APRC↑	SHD↓
10	911	18.969	False	-	-
			True	-	-
15	1274	21.625	False	0.741	29
			True	<b>0.748</b>	<b>12</b>
20	1629	30.219	False	<b>0.731</b>	31
			True	0.723	<b>14</b>
25	1974	30.703	False	0.692	35
			True	<b>0.748</b>	<b>12</b>
30	2319	34.625	False	0.711	38
			True	<b>0.777</b>	<b>11</b>

The **black bold font** is the better score. Downarrow (↓) means lower is better, and vice versa for uparrow (↑).

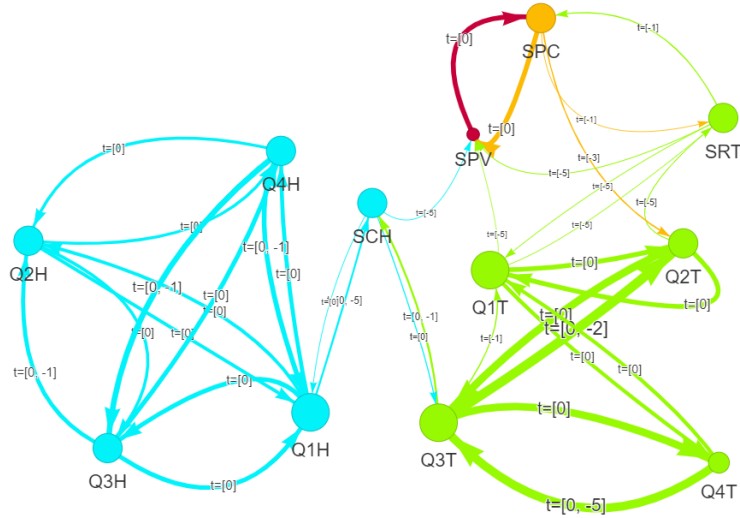


Figure 12: Temporal GCM of HEP07-RM using time-lag  $t = 0, \dots, 5$ .

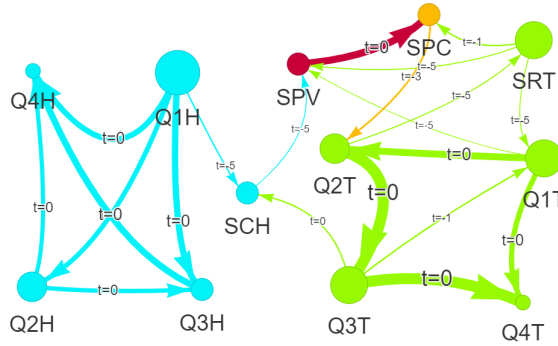


Figure 13: Temporal GCM-DAG network of HEP07-RM after edges pruning.

0.95 on the SPC when anomalies are detected on both the SPV and SRT, indicating the CP is influenced by edge weight strength from multiple causal nodes.

The BN inference has generally produced CPs that are aligned with the link strength of the causal DAG, depicted in Figure 13. But, caution should be taken when approaching the BN causality interpretation: 1) bidirectional edges between Q[1-4]T and Q[1-4]H indicate the presence of confounding variables: the causal sufficiency assumption is not held; the temperature and humidity anomalies are externally induced (affecting the closely placed QIE cards together), and the BN inference depicts the anomaly relationship rather than the causality between the sensors, and 2) the CP, whether it is causal or influenced by observed evidence, must be explained with link edge direction; for example, the CP increase in the SPC is due to the observed anomaly on the causal SPV node, whereas the increase in the SPV is due to the observed anomaly on the influenced SPC node.

## 5.2 Experiment Results on Public Data

We have tested our ANOMALYCD approach on a publicly available dataset [64](see Section 3.2). Assaad et al. [31] has utilized the dataset for a RCA study using a prior known causal graph network of the sensors (see Figure 14).

We generated the anomaly flags dataset using our online AD approach before estimating the GCM of the EasyVista system (see Figure 15a). We have utilized a low threshold  $\alpha_\eta = 2$  to detect more outlier noise beyond the main collective anomaly at indices 46683 to 46783; incorporating the noise outliers improves the CD since the collective anomaly affects all TS variables at the same time, and limits the causality learning from the binary data. The generated binary data contains roughly 4300 samples for each variable, and Figure 15b provide the anomaly flag count; the PMDB and ESB variables generate the highest anomaly flags, and the EasyVista experts consider these two variables to be the root causes of the anomalies.

Table 5: Anomaly conditional probability based on Bayesian causality inference.

Target Variable (A) at $t = 0$	Observed Variables (B)	$\mathcal{P}(A = 1   B = 1)$
Q1T	-	0.051
	Q2T ( $t = 0$ )	0.904
	Q[2-4]T ( $t = 0$ )	0.927
Q1H	-	0.262
	Q2H ( $t = 0$ )	0.846
	Q[2-4]H ( $t = 0$ )	0.913
SPC	-	0.071
	SPV ( $t = 0$ )	0.456
	SRT ( $t = -1$ )	0.321
	SRT ( $t = -5$ )	0.153
	SPV ( $t = 0$ ) and SRT ( $t = -1$ )	0.947
SPV	-	0.057
	SPC ( $t = 0$ )	0.366

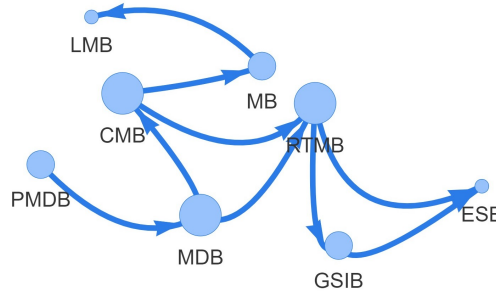


Figure 14: Causal graph of EasyVista’s monitoring system during normal operation.

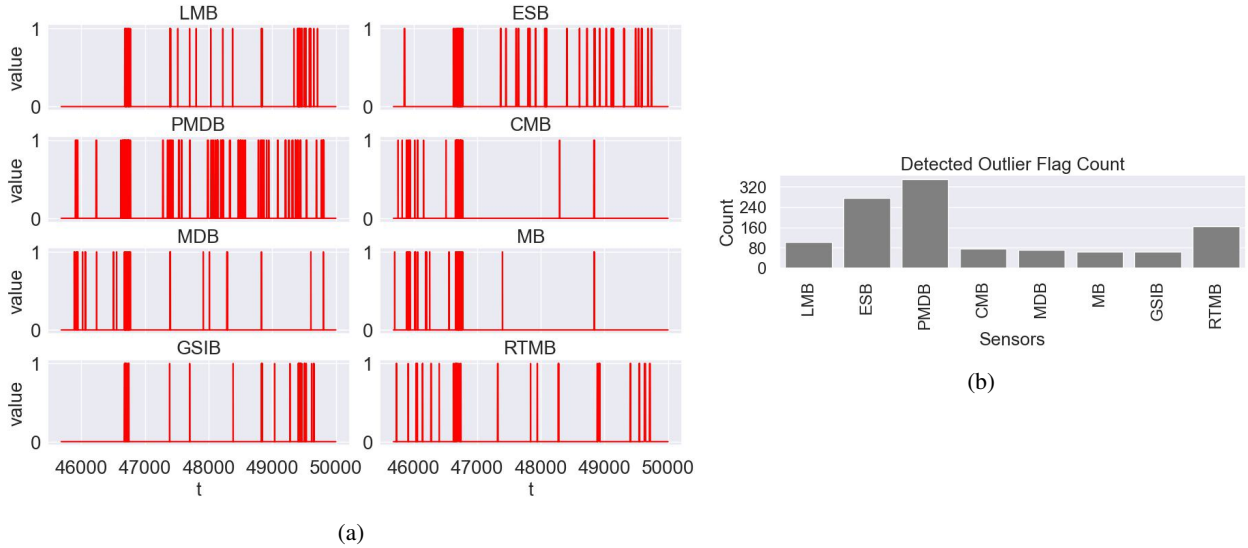


Figure 15: The generated TS anomaly-flag data using our online-AD on the EasyVista sensors.

We utilize the causal graph of the normal operation, given in Figure 14, as a reference graph to evaluate the accuracy of the estimated GCMs. We employ additional metrics for the evaluation to compare the performance of several existing CD approaches:

$$F_1 = \frac{2 \times P \times R}{P + R}, \quad FPR = \frac{RV + FP}{TN + FP}, \quad \text{and} \quad SHDU = UE + UM + RV \quad (14)$$

where the P is precision, R is recall,  $F_1$  is F1-score, and FPR is a false positive rate. The SHDU is *undirected SHD* that penalizes once for edges with wrong directions instead of twice as SHD in Eq. (12) [79]. The TP, TN, FP, and FN stand

for true positive, true negative, false positive, and false negative, respectively (see definition in Eq. (13)). The RV, UE, and UM denote the number of reversed edges, undirected extra edges, and undirected missing edges, respectively.

Table 6 presents some of the popular CD methods in the literature and used in our study for comparison. We have preserved the undirected edges as bidirected for a fair comparison among the methods since some of the methods generate PDAG. We convert the temporal GCM results into summary GCM for the PCMCI-based temporal CD since the evaluation reference graph does not contain temporal information; we aggregate the time lag attributes of the edges into  $t = 0$ . We utilize partial correlation for the CI testing and  $p_v = 0.05$  for the constraint-based methods. We employ *BiC* and *BDeu* scores [80] for the score-based algorithms.

Table 6: Causal discovery methods.

Method Category	List of Methods
Constraint-based	PC [42], GS [39], IAMP [40], MMPC [41], PCMCI [24]
Score-based	HC [44], GES [45]
Hybrid-based	MMHC [43]
Function-based	Direct-LiNGAM [81], ICA-LiNGAM [82]
Gradient-based	GraN-DAG [83], GOLEM [84], GAE [85], RL-BIC [86], CORL [87]

Table 7 and Table 8 provide the CD performance on the raw binary anomaly data and compressed data by sparse handling algorithm, respectively. Most methods have reached higher R with lower P scores due to the bi-directed edges. Only the graph autoencoder (GAE) [85] has succeeded from the DL models; the RL-BIC [86] and CORL [87] employs reinforcement learning and have missed all relevant edges that require a wider search for optimal hyper-parameters to improve the performance. The sparse handler reduces the input data size by 55% using  $l_m = 10$ , which leads to lower computation. It also decreases the number of estimated edges, which improves the accuracy of the causal graph; it increases the  $F_1$  by improving the precision and reducing the false edges, which also decreases the SHD and SHDU. The score-based HC [44] and its hybrid MMHC [43] algorithms have not provided accuracy leverage on the compressed binary data. Our sparse handling method achieves an average relative improvement, compared to raw data in Table 7 and excluding the HC and MMHC algorithms, of 18.31%, 22.05%, and 15.45% in the  $F_1$ , FPR, and SHDU, respectively (see Table 8).

Our ANOMALYCD leads the performance in most metrics and is ranked first by the Nemenyi ranking diagram [88] over the rank scores across the seven metrics (see Figure 16). The CD accuracy is not very high overall across the different approaches. This might be because the reference system GCM used for the evaluation is derived from normal operations, and the anomaly GCM, built from the anomaly data, may behave differently.

Table 7: Causal graph learning on EasyVista dataset without sparse data handling.

Metric	P $\uparrow$	R $\uparrow$	F $_1\uparrow$	FPR $\downarrow$	APRC $\uparrow$	SHD $\downarrow$	SHDU $\downarrow$
PC [42]	0.118	0.222	0.154	0.790	0.225	34	18
GS [39]	0.174	<b>0.889</b>	0.291	0.790	<b>0.539</b>	56	16
IAMB [40]	0.174	<b>0.889</b>	0.291	0.790	<b>0.539</b>	56	16
MMPC [41]	0.174	<b>0.889</b>	0.291	0.790	<b>0.539</b>	56	16
HC-BicScore [44]	0.167	0.222	0.191	0.526	0.249	45	13
HC-BdeuScore [44]	<b>0.222</b>	0.444	0.296	0.737	0.372	<b>21</b>	17
GES-BicScore [45]	0.160	0.444	0.235	0.895	0.341	35	18
GES-BdeuScore [45]	0.191	0.444	0.267	0.526	0.357	48	15
MMHC [43]	0.182	0.222	0.200	0.474	0.257	44	<b>12</b>
Direct-LiNGAM [81]	0.167	0.444	0.242	1.050	0.345	37	21
ICA-LiNGAM [82]	0.160	0.444	0.235	1.105	0.341	33	22
GOLEM [84]	0.167	0.222	0.191	0.526	0.249	35	16
GraN-DAG [83]	<b>0.222</b>	0.222	0.222	<b>0.368</b>	0.277	38	13
GAE [85]	0.177	0.333	0.231	0.421	0.302	47	14
PCMCI [24]	0.182	<b>0.889</b>	0.302	0.895	0.543	50	17
ANOMALYCD (ours)	0.212	0.778	<b>0.333</b>	0.684	0.511	48	13

The **black bold font** is the best score. Downarrow ( $\downarrow$ ) means lower is better, and vice versa for uparrow ( $\uparrow$ ).

We present an ablation study in Table 9 for the ANOMALYCD approach to demonstrate the efficacy of the additional complexity using ANAC, sparse handling, and temporal edge pruning methods leveraging the PCMCI algorithm [24]. ANOMALYCD has enhanced the CD by 20% in the  $F_1$  score. The P, FPR, and SHDU are substantially improved by 37%, 47%, and 41%, respectively, demonstrating improved link detection accuracy. The performance decrease on the SHD by 7% relative to ANOMALYCD\*\* is due to the slight accuracy drop in the direction estimation of the bi-directed

Table 8: Causal graph learning on EasyVista dataset with our sparse data handling method. The  $\Delta_{\text{avg}}^+$  and  $\Delta_{\text{avg}}^-$  are the average relative gains (compared to the performance on the raw data, given in Table 7) of our sparse data handling method over all the CD algorithms, including and excluding the low-performing HC and MMHC algorithms, respectively.

Metric	P $\uparrow$	R $\uparrow$	F $_1\uparrow$	FPR $\downarrow$	APRC $\uparrow$	SHD $\downarrow$	SHDU $\downarrow$
PC [42]	<b>0.267</b>	0.444	0.333	0.474	0.395	29	12
GS [39]	0.191	0.444	0.267	0.632	0.357	47	15
IAMB [40]	0.191	0.444	0.267	0.632	0.357	47	15
MMPC [41]	0.200	<b>0.667</b>	0.308	0.474	0.457	54	12
HC-BicScore [44]	0.091	0.111	0.100	0.526	0.164	35	15
HC-BdeuScore [44]	0.111	0.222	0.148	0.842	0.221	32	19
GES-BicScore [45]	0.227	0.556	0.323	0.632	0.423	36	14
GES-BdeuScore [45]	0.191	0.444	0.267	0.526	0.357	48	15
MMHC [43]	0.100	0.111	0.105	0.474	0.168	47	14
Direct-LiNGAM [81]	0.167	0.333	0.222	0.790	0.297	38	17
ICA-LiNGAM [82]	0.235	0.444	0.308	0.684	0.379	<b>22</b>	16
GOLEM [84]	0.167	0.222	0.191	0.526	0.249	35	16
GraN-DAG [84]	0.333	0.333	0.333	<b>0.316</b>	0.380	36	12
GAE [85]	0.200	0.333	0.250	0.421	0.314	41	13
PCMCI [24]	0.207	<b>0.667</b>	0.316	0.632	0.460	52	13
ANOMALYCD (ours)	0.250	<b>0.667</b>	<b>0.364</b>	0.474	<b>0.482</b>	44	<b>10</b>
$\Delta_{\text{avg}}^+$ (%)	<b>12.72</b>	<b>-10.26</b>	<b>5.80</b>	<b>17.03</b>	<b>-4.69</b>	<b>3.97</b>	<b>9.81</b>
$\Delta_{\text{avg}}^-$ (%)	<b>26.47</b>	<b>-1.08</b>	<b>18.31</b>	<b>22.05</b>	<b>2.64</b>	<b>7.74</b>	<b>15.45</b>

The **green** and **red bold font** represent an increase and decrease in performance, respectively.

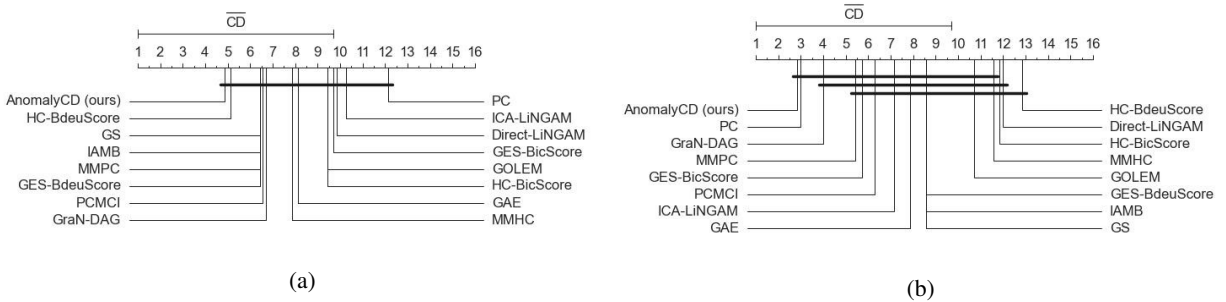


Figure 16: Performance ranking for pairwise comparisons using Nemenyi: a) without sparse data handling, and b) with sparse data handling. The CD is the *critical difference distance*, and the horizontal bars denote mean rank differences smaller than the value of the CD.

edges at  $t = 0$  (see Figure 17). The correlation-based CI test may remain symmetric and unable to distinguish edge direction at  $t = 0$  when there is no time-lagged factor, see Eq. (11). The ANOMALYCD-Directed refers ANOMALYCD with updated edges using chi-square test for the bi-directed edges, line 17 in Algorithm 4 (see Figure 17b). The ANOMALYCD-Directed attains the best performance in most metrics, improving the CD over the PCMCI by 83%, 26%, 53%, 36%, and 41%, in the P, F $_1$ , FPR, SHD, and SHDU, respectively. The decrease in the R is because some of the bi-directed edges are removed or direction reversed by the pruning chi-square test.

Table 9: Ablation study on our ANOMALYCD approach using the EasyVista dataset. ANOMALYCD is our proposed temporal CD with ANAC, sparse handling, and edge pruning, ANOMALYCD\* is without sparse handling, ANOMALYCD\*\* is with ANAC, and ANOMALYCD\*\*\* is without sparse handling and edge pruning, equivalent to the PCMCI algorithm in Ref. [24]. The ANOMALYCD-Directed is ANOMALYCD with directed edges.

Metric	P $\uparrow$	R $\uparrow$	F $_1\uparrow$	FPR $\downarrow$	APRC $\uparrow$	SHD $\downarrow$	SHDU $\downarrow$
ANOMALYCD-Directed	<b>0.333</b>	0.444	<b>0.381</b>	<b>0.421</b>	0.428	<b>32</b>	<b>10</b>
ANOMALYCD	0.250	0.667	0.364	0.474	0.482	44	<b>10</b>
ANOMALYCD*	0.212	0.778	0.333	0.684	0.511	48	13
ANOMALYCD**	0.184	0.778	0.298	0.947	0.497	41	18
ANOMALYCD*** [24]	0.182	<b>0.889</b>	0.302	0.895	<b>0.543</b>	50	17



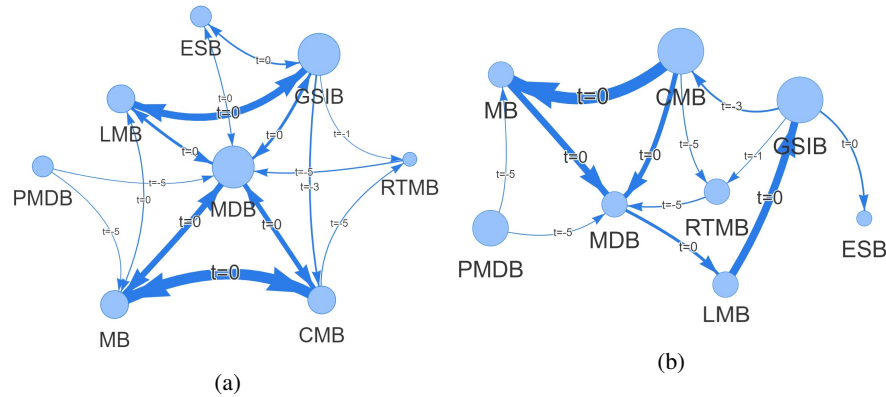


Figure 17: The estimated TS GCM using ANOMALYCD for the EasyVista system from binary anomaly data: a) ANOMALYCD, and b) ANOMALYCD-Directed.

## 6 Conclusion

We have developed a scalable framework for discovering causal graphs using computationally efficient methods with binary anomaly flag datasets. Our framework incorporates various approaches to tackle the computational and accuracy challenges of inferring causality in sparse binary anomaly data. We have systematically integrated the characteristics of anomaly flag data into causal condition testing, sparse data compression, link compression based on prior time-lag assumptions, and pruning adjustments to improve computation and accuracy. The results of our experiments have demonstrated promising accuracy in unsupervised online anomaly detection and a significant reduction in the computational overhead associated with causal graph discovery on monitoring time series data sets. Our approaches will facilitate diagnostic tasks across various subsystems of large systems, such as the Hadron Calorimeter and other sectors related to Industry 4.0, addressing the demand for flexible, unsupervised, and lightweight approaches that are capable of handling complex system configurations with limited annotated data sets. The causal networks identified from the anomaly data can be further analyzed to identify root causes using various established methods. However, it is essential to first define the time course of the target anomaly before learning the causal graph, as different anomalies may have distinct root causes. The tools presented in this study are deployed at the Compact Muon Solenoid experiment at CERN’s Large Hadron Collider to provide diagnostics for the Hadron Calorimeter systems.

## Acknowledgment

We sincerely appreciate the CMS collaboration, the HCAL operation group, the HCAL publication committee, and the CMS machine learning teams. Their technical expertise, diligent follow-up on our work, and thorough manuscript review have been invaluable. We also thank the collaborators for building and maintaining the detector systems used in our study. We extend our appreciation to the CERN for the operations of the LHC accelerator. The teams at CERN have also received support from the Belgian Fonds de la Recherche Scientifique, and Fonds voor Wetenschappelijk Onderzoek; the Brazilian Funding Agencies (CNPq, CAPES, FAPERJ, FAPERGS, and FAPESP); SRNSF (Georgia); the Bundesministerium für Bildung und Forschung, the Deutsche Forschungsgemeinschaft (DFG), under Germany’s Excellence Strategy – EXC 2121 “Quantum Universe” – 390833306, and under project number 400140256 - GRK2497, and Helmholtz-Gemeinschaft Deutscher Forschungszentren, Germany; the National Research, Development and Innovation Office (NKFIH) (Hungary) under project numbers K 128713, K 143460, and TKP2021-NKTA-64; the Department of Atomic Energy and the Department of Science and Technology, India; the Ministry of Science, ICT and Future Planning, and National Research Foundation (NRF), Republic of Korea; the Lithuanian Academy of Sciences; the Scientific and Technical Research Council of Turkey, and Turkish Energy, Nuclear and Mineral Research Agency; the National Academy of Sciences of Ukraine; the US Department of Energy.

## References

- [1] B. Rashidi, D. S. Singh, and Q. Zhao, “Data-driven root-cause fault diagnosis for multivariate non-linear processes,” *Control Engineering Practice*, vol. 70, pp. 134–147, 2018.
- [2] V. Leonhardt, F. Claus, and C. Garth, “PEN: process estimator neural network for root cause analysis using graph convolution,” *Journal of Manufacturing Systems*, vol. 62, pp. 886–902, 2022.

- [3] A. Gerhardus and J. Runge, “High-recall causal discovery for autocorrelated time series with latent confounders,” *Advances in Neural Information Processing Systems*, vol. 33, pp. 12 615–12 625, 2020.
- [4] B. Steenwinckel, D. De Paepe, S. V. Haute, P. Heyvaert, M. Bentefrit, P. Moens, A. Dimou, B. Van Den Bossche, F. De Turck, S. Van Hoecke *et al.*, “FLAGS: a methodology for adaptive anomaly detection and root cause analysis on sensor data streams by fusing expert knowledge with machine learning,” *Future Generation Computer Systems*, vol. 116, pp. 30–48, 2021.
- [5] J. Martinez-Gil, G. Buchgeher, D. Gabauer, B. Freudenthaler, D. Filipiak, and A. Fensel, “Root cause analysis in the industrial domain using knowledge graphs: a case study on power transformers,” *Procedia Computer Science*, vol. 200, pp. 944–953, 2022.
- [6] C. Glymour, K. Zhang, and P. Spirtes, “Review of causal discovery methods based on graphical models,” *Frontiers in genetics*, vol. 10, p. 524, 2019.
- [7] R. Guo, L. Cheng, J. Li, P. R. Hahn, and H. Liu, “A survey of learning causality with data: problems and methods,” *ACM Computing Surveys*, vol. 53, no. 4, pp. 1–37, 2020.
- [8] C. Liu, K. G. Lore, Z. Jiang, and S. Sarkar, “Root-cause analysis for time-series anomalies via spatiotemporal graphical modeling in distributed complex systems,” *Knowledge-Based Systems*, vol. 211, p. 106527, 2021.
- [9] K. Böhmer and S. Rinderle-Ma, “Mining association rules for anomaly detection in dynamic process runtime behavior and explaining the root cause to users,” *Information Systems*, vol. 90, p. 101438, 2020.
- [10] C. Tian, C. Zhao, H. Fan, and Z. Zhang, “Causal network construction based on convergent cross mapping (ccm) for alarm system root cause tracing of nonlinear industrial process,” *IFAC-PapersOnLine*, vol. 53, no. 2, pp. 13 619–13 624, 2020.
- [11] M. Nauta, D. Bucur, and C. Seifert, “Causal discovery with attention-based convolutional neural networks,” *Machine Learning and Knowledge Extraction*, vol. 1, no. 1, pp. 312–340, 2019.
- [12] Y. Zhou, K. Xu, and F. He, “Root cause diagnosis in multivariate time series based on modified temporal convolution and multi-head self-attention,” *Journal of Process Control*, vol. 117, pp. 14–25, 2022.
- [13] M. W. Asres, G. Cummings, P. Parygin, A. Khukhunaishvili, M. Toms, A. Campbell, S. I. Cooper, D. Yu, J. Dittmann, and C. W. Omlin, “Unsupervised deep variational model for multivariate sensor anomaly detection,” in *International Conference on Progress in Informatics and Computing*. IEEE, 2021, pp. 364–371.
- [14] M. W. Asres, G. Cummings, A. Khukhunaishvili, P. Parygin, S. I. Cooper, D. Yu, J. Dittmann, and C. W. Omlin, “Long horizon anomaly prediction in multivariate time series with causal autoencoders,” in *PHM Society European Conference*, vol. 7, no. 1, 2022, pp. 21–31.
- [15] M. W. Asres, C. W. Omlin, L. Wang, D. Yu, P. Parygin, J. Dittmann, G. Karapostoli, M. Seidel, R. Venditti, L. Lambrecht *et al.*, “Spatio-temporal anomaly detection with graph networks for data quality monitoring of the Hadron Calorimeter,” *Sensors*, vol. 23, no. 24, p. 9679, 2023.
- [16] M. W. Asres, C. W. Omlin, L. Wang, P. Parygin, D. Yu, J. Dittmann, and The CMS-HCAL Collaboration, “Data quality monitoring through transfer learning on anomaly detection for the Hadron Calorimeters,” *arXiv preprint arXiv:2408.16612*, 2024.
- [17] A. A. Pol, V. Azzolini, G. Cerminara, F. De Guio, G. Franzoni, M. Pierini, F. Sirokỳ, and J.-R. Vlimant, “Anomaly detection using deep autoencoders for the assessment of the quality of the data acquired by the CMS experiment,” in *European Physical Journal Web of Conferences*, vol. 214. EDP Sciences, 2019, p. 06008.
- [18] M. Wielgosz, M. Mertik, A. Skoczeń, and E. De Matteis, “The model of an anomaly detector for HiLumi LHC magnets based on recurrent neural networks and adaptive quantization,” *Engineering Applications of Artificial Intelligence*, vol. 74, pp. 166–185, 2018.
- [19] D. Abadjiev, “Autoencoder-based anomaly detection system for online data quality monitoring of the cms electromagnetic calorimeter,” Fermi National Accelerator Laboratory (FNAL), Batavia, IL (United States), Tech. Rep., 2023.
- [20] C. Amornbunchornvej, N. Surasvadi, A. Plangprasopchok, and S. Thajchayapong, “Framework for inferring empirical causal graphs from binary data to support multidimensional poverty analysis,” *Heliyon*, vol. 9, no. 5, 2023.
- [21] K. Budhathoki, L. Minorics, P. Blöbaum, and D. Janzing, “Causal structure-based root cause analysis of outliers,” in *International Conference on Machine Learning*. Proceedings of Machine Learning Research, 2022, pp. 2357–2369.
- [22] J. Runge, “Causal network reconstruction from time series: from theoretical assumptions to practical estimation,” *Chaos: an Interdisciplinary Journal of Nonlinear Science*, vol. 28, no. 7, 2018.
- [23] J. Runge, P. Nowack, M. Kretschmer, S. Flaxman, and D. Sejdinovic, “Detecting and quantifying causal associations in large nonlinear time series datasets,” *Science Advances*, vol. 5, no. 11, p. eaau4996, 2019.
- [24] J. Runge, “Discovering contemporaneous and lagged causal relations in autocorrelated nonlinear time series datasets,” in *Conference on Uncertainty in Artificial Intelligence*. Proceedings of Machine Learning Research, 2020, pp. 1388–1397.
- [25] E. Saggioro, J. de Wiljes, M. Kretschmer, and J. Runge, “Reconstructing regime-dependent causal relationships from observational time series,” *Chaos: an Interdisciplinary Journal of Nonlinear Science*, vol. 30, no. 11, 2020.
- [26] R. E. Neapolitan *et al.*, *Learning Bayesian networks*. Pearson Prentice Hall, 2004, vol. 38.

- [27] P. Wang, J. Xu, M. Ma, W. Lin, D. Pan, Y. Wang, and P. Chen, "CloudRanger: root cause identification for cloud native systems," in *18th International Symposium on Cluster, Cloud and Grid Computing*. IEEE, 2018, pp. 492–502.
- [28] Y. Meng, S. Zhang, Y. Sun, R. Zhang, Z. Hu, Y. Zhang, C. Jia, Z. Wang, and D. Pei, "Localizing failure root causes in a microservice through causality inference," in *28th International Symposium on Quality of Service*. IEEE, 2020, pp. 1–10.
- [29] P. Spirtes, C. N. Glymour, and R. Scheines, *Causation, prediction, and search*. MIT press, 2000.
- [30] M. Chevalley, Y. Roohani, A. Mehrjou, J. Leskovec, and P. Schwab, "CausalBench: a large-scale benchmark for network inference from single-cell perturbation data," *arXiv preprint arXiv:2210.17283*, 2022.
- [31] C. K. Assaad, I. Ez-Zejjari, and L. Zan, "Root cause identification for collective anomalies in time series given an acyclic summary causal graph with loops," in *International Conference on Artificial Intelligence and Statistics*. Proceedings of Machine Learning Research, 2023, pp. 8395–8404.
- [32] J. Chen and C. Zhao, "Multi-lag and multi-type temporal causality inference and analysis for industrial process fault diagnosis," *Control Engineering Practice*, vol. 124, p. 105174, 2022.
- [33] Q. Chen, X. Lang, S. Lu, N. ur Rehman, L. Xie, and H. Su, "Detection and root cause analysis of multiple plant-wide oscillations using multivariate nonlinear chirp mode decomposition and multivariate Granger causality," *Computers and Chemical Engineering*, vol. 147, p. 107231, 2021.
- [34] K. Qin, L. Chen, J. Shi, Z. Li, and K. Hao, "Root cause analysis of industrial faults based on binary extreme gradient boosting and temporal causal discovery network," *Chemometrics and Intelligent Laboratory Systems*, vol. 225, p. 104559, 2022.
- [35] N. Liu, M. Hu, J. Wang, Y. Ren, and W. Tian, "Fault detection and diagnosis using bayesian network model combining mechanism correlation analysis and process data: application to unmonitored root cause variables type faults," *Process Safety and Environmental Protection*, vol. 164, pp. 15–29, 2022.
- [36] D. De Paepe, S. V. Hautebe, B. Steenwinckel, F. De Turck, F. Ongenaes, O. Janssens, and S. Van Hoecke, "A generalized matrix profile framework with support for contextual series analysis," *Engineering Applications of Artificial Intelligence*, vol. 90, p. 103487, 2020.
- [37] K. Budhathoki, D. Janzing, P. Bloebaum, and H. Ng, "Why did the distribution change?" in *International Conference on Artificial Intelligence and Statistics*. Proceedings of Machine Learning Research, 2021, pp. 1666–1674.
- [38] S. M. Lundberg and S.-I. Lee, "A unified approach to interpreting model predictions," in *Advances in Neural Information Processing Systems*. Curran Associates, Inc., 2017, vol. 30, pp. 4765–4774.
- [39] D. Margaritis *et al.*, "Learning bayesian network model structure from data," Ph.D. dissertation, School of Computer Science, Carnegie Mellon University Pittsburgh, PA, USA, 2003.
- [40] I. Tsamardinos, C. F. Aliferis, A. R. Statnikov, and E. Statnikov, "Algorithms for large scale Markov blanket discovery," in *FLAIRS conference*, vol. 2. St. Augustine, FL, 2003, pp. 376–380.
- [41] I. Tsamardinos, C. F. Aliferis, and A. Statnikov, "Time and sample efficient discovery of Markov blankets and direct causal relations," in *Proceedings of the 9th ACM SIGKDD International Conference on Knowledge Discovery and Data Mining*, 2003, pp. 673–678.
- [42] D. Colombo, M. H. Maathuis *et al.*, "Order-independent constraint-based causal structure learning," *Journal of Machine Learning Research*, vol. 15, no. 1, pp. 3741–3782, 2014.
- [43] I. Tsamardinos, L. E. Brown, and C. F. Aliferis, "The max-min hill-climbing bayesian network structure learning algorithm," *Machine Learning*, vol. 65, pp. 31–78, 2006.
- [44] D. Koller and N. Friedman, *Probabilistic graphical models: principles and techniques*. MIT press, 2009.
- [45] D. M. Chickering, "Optimal structure identification with greedy search," *Journal of machine learning research*, vol. 3, no. Nov, pp. 507–554, 2002.
- [46] J. D. Ramsey, "Scaling up greedy causal search for continuous variables," *arXiv preprint arXiv:1507.07749*, 2015.
- [47] J. M. Ogarrio, P. Spirtes, and J. Ramsey, "A hybrid causal search algorithm for latent variable models," in *Conference on Probabilistic Graphical Models*. Proceedings of Machine Learning Research, 2016, pp. 368–379.
- [48] P. Bühlmann, J. Peters, and J. Ernest, "CAM: causal additive models, high-dimensional order search and penalized regression," *The Annals of Statistics*, vol. 42, pp. 2526–2556, 2014.
- [49] O. Goudet, D. Kalainathan, P. Caillou, I. Guyon, D. Lopez-Paz, and M. Sebag, "Learning functional causal models with generative neural networks," *Explainable and Interpretable Models in Computer Vision and Machine Learning*, pp. 39–80, 2018.
- [50] J. Peters, D. Janzing, and B. Schölkopf, *Elements of causal inference: foundations and learning algorithms*. The MIT Press, 2017.
- [51] Y. Liu, H.-S. Chen, H. Wu, Y. Dai, Y. Yao, and Z. Yan, "Simplified granger causality map for data-driven root cause diagnosis of process disturbances," *Journal of Process Control*, vol. 95, pp. 45–54, 2020.
- [52] A. Shojaie and E. B. Fox, "Granger causality: a review and recent advances," *Annual Review of Statistics and Its Application*, vol. 9, pp. 289–319, 2022.

- [53] R. Biswas and E. Shlizerman, “Statistical perspective on functional and causal neural connectomics: the time-aware pc algorithm,” *PLOS Computational Biology*, vol. 18, no. 11, p. e1010653, 2022.
- [54] C. W. Granger, “Investigating causal relations by econometric models and cross-spectral methods,” *Econometrica: Journal of the Econometric Society*, pp. 424–438, 1969.
- [55] A. Tank, I. Covert, N. Foti, A. Shojaie, and E. B. Fox, “Neural Granger causality,” *IEEE Transactions on Pattern Analysis and Machine Intelligence*, vol. 44, no. 8, pp. 4267–4279, 2021.
- [56] The CMS Collaboration, S. Chatrchyan, G. Hmayakyan, V. Khachatryan, A. Sirunyan, W. Adam, T. Bauer, T. Bergauer, H. Bergauer, M. Dragicevic *et al.*, “The CMS experiment at the CERN LHC,” *Journal of Instrumentation*, vol. 3, p. S08004, 2008.
- [57] A. Hayrapetyan *et al.*, “Development of the CMS detector for the CERN LHC Run 3,” *JINST*, vol. 19, no. 05, p. P05064, 2024.
- [58] N. Strobbe, “The upgrade of the CMS Hadron Calorimeter with Silicon photomultipliers,” *Journal of Instrumentation*, vol. 12, no. 1, p. C01080, 2017.
- [59] E. Focardi, “Status of the CMS detector,” *Physics Procedia*, vol. 37, pp. 119–127, 2012.
- [60] J. Mans, “CMS technical design report for the phase 1 upgrade of the hadron calorimeter,” CMS-TDR-010, Tech. Rep., 2012.
- [61] G. Baiatian, M. Hashemi, S. Hagopian, A. Pal, E. Machado, E. Isiksal, V. O’Dell, T. Haelen, D. A. Sanders, E. Yazgan *et al.*, “Design, performance, and calibration of CMS Hadron Endcap calorimeters,” CERN-CMS-NOTE-2008-010, Tech. Rep., 2008.
- [62] M. W. Asres, C. W. Omlin, J. Dittmann, P. Parygin, J. Hiltbrand, S. I. Cooper, G. Cummings, and D. Yu, “Lightweight multi-system multivariate interconnection and divergence discovery,” in *19th Annual System of Systems Engineering Conference (SoSE)*, 2024.
- [63] “EasyVista,” <https://www.easyvista.com/fr/produits/ev-observe>, accessed: 2023-01-10.
- [64] “EasyRCA IT monitoring dataset,” <https://github.com/ckassaad/EasyRCA>, accessed: 2023-01-10.
- [65] F. Karim, S. Majumdar, H. Darabi, and S. Harford, “Multivariate LSTM-FCNs for time series classification,” *Neural Networks*, vol. 116, pp. 237–245, 2019.
- [66] R. B. Cleveland, W. S. Cleveland, J. E. McRae, and I. Terpenning, “STL: a seasonal-trend decomposition,” *J. Off. Stat.*, vol. 6, no. 1, pp. 3–73, 1990.
- [67] T. Puech, M. Boussard, A. D’Amato, and G. Millerand, “A fully automated periodicity detection in time series,” in *Advanced Analytics and Learning on Temporal Data: 4th ECML PKDD Workshop*. Springer, 2020, pp. 43–54.
- [68] A. Ermshaus, P. Schäfer, and U. Leser, “ClaSP: parameter-free time series segmentation,” *Data Mining and Knowledge Discovery*, vol. 37, no. 3, pp. 1262–1300, 2023.
- [69] K. Bandara, R. J. Hyndman, and C. Bergmeir, “MSTL: a seasonal-trend decomposition algorithm for time series with multiple seasonal patterns,” *arXiv preprint arXiv:2107.13462*, 2021.
- [70] H. Ren, B. Xu, Y. Wang, C. Yi, C. Huang, X. Kou, T. Xing, M. Yang, J. Tong, and Q. Zhang, “Time-series anomaly detection service at Microsoft,” in *Proceedings of the 25th ACM SIGKDD International Conference on Knowledge Discovery and Data Mining*, 2019, pp. 3009–3017.
- [71] W. Niu, Z. Gao, L. Song, and L. Li, “Comprehensive review and empirical evaluation of causal discovery algorithms for numerical data,” *arXiv preprint arXiv:2407.13054*, 2024.
- [72] L. Castri, S. Mghames, M. Hanheide, and N. Bellotto, “Enhancing causal discovery from robot sensor data in dynamic scenarios,” in *Conference on Causal Learning and Reasoning*. PMLR, 2023, pp. 243–258.
- [73] Y. M. Bishop, S. E. Fienberg, and P. W. Holland, *Discrete multivariate analysis: theory and practice*. Springer Science and Business Media, 2007.
- [74] K. P. Murphy, *Dynamic Bayesian networks: representation, inference and learning*. University of California, Berkeley, 2002.
- [75] A. Sheidaei, A. R. Foroushani, K. Gohari, and H. Zeraati, “A novel dynamic Bayesian network approach for data mining and survival data analysis,” *BMC Medical Informatics and Decision Making*, vol. 22, no. 1, pp. 1–15, 2022.
- [76] R. Killick, P. Fearnhead, and I. A. Eckley, “Optimal detection of changepoints with a linear computational cost,” *Journal of the American Statistical Association*, vol. 107, no. 500, pp. 1590–1598, 2012.
- [77] A. Celisse, G. Marot, M. Pierre-Jean, and G. Rigaiil, “New efficient algorithms for multiple change-point detection with reproducing kernels,” *Computational Statistics and Data Analysis*, vol. 128, pp. 200–220, 2018.
- [78] J. Peters and P. Bühlmann, “Structural intervention distance for evaluating causal graphs,” *Neural Computation*, vol. 27, no. 3, pp. 771–799, 2015.
- [79] K. Zhang, S. Zhu, M. Kalander, I. Ng, J. Ye, Z. Chen, and L. Pan, “gcastle: a python toolbox for causal discovery,” *arXiv preprint arXiv:2111.15155*, 2021.
- [80] A. M. Carvalho, “Scoring functions for learning bayesian networks,” *Inesc-id Tec. Rep.*, vol. 12, pp. 1–48, 2009.
- [81] S. Shimizu, T. Inazumi, Y. Sogawa, A. Hyvarinen, Y. Kawahara, T. Washio, P. O. Hoyer, K. Bollen, and P. Hoyer, “DirectLiNGAM: a direct method for learning a linear non-Gaussian structural equation model,” *Journal of Machine Learning Research*, vol. 12, no. Apr, pp. 1225–1248, 2011.

- [82] S. Shimizu, P. O. Hoyer, A. Hyvärinen, A. Kerminen, and M. Jordan, “A linear non-Gaussian acyclic model for causal discovery,” *Journal of Machine Learning Research*, vol. 7, no. 10, 2006.
- [83] S. Lachapelle, P. Brouillard, T. Deleu, and S. Lacoste-Julien, “Gradient-based neural dag learning,” *arXiv preprint arXiv:1906.02226*, 2019.
- [84] I. Ng, A. Ghassami, and K. Zhang, “On the role of sparsity and dag constraints for learning linear dags,” *Advances in Neural Information Processing Systems*, vol. 33, pp. 17 943–17 954, 2020.
- [85] I. Ng, S. Zhu, Z. Chen, and Z. Fang, “A graph autoencoder approach to causal structure learning,” *arXiv preprint arXiv:1911.07420*, 2019.
- [86] S. Zhu, I. Ng, and Z. Chen, “Causal discovery with reinforcement learning,” *arXiv preprint arXiv:1906.04477*, 2019.
- [87] X. Wang, Y. Du, S. Zhu, L. Ke, Z. Chen, J. Hao, and J. Wang, “Ordering-based causal discovery with reinforcement learning,” *arXiv preprint arXiv:2105.06631*, 2021.
- [88] P. B. Nemenyi, *Distribution-free multiple comparisons*. Princeton University, 1963.



## The CMS-HCAL Collaboration

M.W. Asres<sup>1</sup>, C.W. Omlin<sup>1</sup>, V. Chekhovskiy<sup>2,a</sup>, A. Chinaryan<sup>2</sup>, A. Gevorgyan<sup>2</sup>, Ya. Halkin<sup>2</sup>, A. Kunts<sup>2</sup>, A. Litomin<sup>2,a</sup>, A. Petrosyan<sup>2</sup>, A. Tumasyan<sup>2</sup>, H. Saka<sup>3</sup>, A. Steppenov<sup>3</sup>, G. Karapostoli<sup>4</sup>, A. Campbell<sup>5</sup>, F. Engelke<sup>5</sup>, M. Csanád<sup>6</sup>, A. Feherkuti<sup>6,b</sup>, G. Pásztor<sup>6</sup>, G.I. Veres<sup>6</sup>, S. Bhattacharya<sup>7</sup>, M.M. Ameen<sup>8,c</sup>, M. Guchait<sup>8</sup>, G. Majumder<sup>8</sup>, K. Mazumdar<sup>8,d</sup>, M. Patil<sup>8</sup>, A. Thachayath<sup>8</sup>, T. Mishra<sup>9,e</sup>, P. Sadangi<sup>9</sup>, H. Hwang<sup>10</sup>, J. Padmanaban<sup>10</sup>, J. Yoo<sup>10</sup>, D. Agyel<sup>11</sup>, Z. Azimi<sup>11</sup>, I. Dumanoglu<sup>11,f</sup>, E. Eskut<sup>11</sup>, Y. Guler<sup>11,g</sup>, E. Gurpinar Guler<sup>11,g</sup>, C. Isik<sup>11</sup>, O. Kara<sup>11</sup>, A. Kayis Topaksu<sup>11</sup>, G. Onengut<sup>11,d</sup>, K. Ozdemir<sup>11,h</sup>, A. Polatoz<sup>11</sup>, B. Tali<sup>11,i</sup>, U.G. Tok<sup>11</sup>, E. Uslan<sup>11</sup>, I.S. Zorbakir<sup>11</sup>, B. Akgun<sup>12</sup>, I.O. Atakisi<sup>12</sup>, B. Gonultas<sup>12</sup>, E. Gülmez<sup>12</sup>, M. Kaya<sup>12,j</sup>, O. Kaya<sup>12,k</sup>, S. Tekten<sup>12,l</sup>, E.A. Yetkin<sup>12,m</sup>, B. Balci<sup>13</sup>, K. Cankocak<sup>13,f</sup>, G.G. Dincer<sup>13</sup>, Y. Komurcu<sup>13</sup>, I. Ozsahin<sup>13</sup>, S. Sen<sup>13,n</sup>, S. Cerci<sup>14</sup>, A.A. Guvenli<sup>14</sup>, E. Iren<sup>14,o</sup>, B. Isildak<sup>14</sup>, O.B. Kolcu<sup>14,p</sup>, E. Simsek<sup>14,q</sup>, D. Sunar Cerci<sup>14</sup>, T. Yetkin<sup>14,p</sup>, B. Hacisahinoglu<sup>15</sup>, I. Hos<sup>15,r</sup>, B. Kaynak<sup>15</sup>, S. Ozkorucuklu<sup>15</sup>, O. Potok<sup>15</sup>, H. Sert<sup>15</sup>, C. Simsek<sup>15</sup>, C. Zorbilmez<sup>15</sup>, L. Levchuk<sup>16</sup>, V. Popov<sup>16</sup>, S. Abdullin<sup>17</sup>, H. Buttrum<sup>17</sup>, J. Dittmann<sup>17</sup>, T. Efthymiadou<sup>17</sup>, K. Hatakeyama<sup>17</sup>, J. Hiltbrand<sup>17</sup>, A. Kalinin<sup>17,a</sup>, J. Wilson<sup>17</sup>, P. Bunin<sup>18,a</sup>, S.I. Cooper<sup>18</sup>, C. Crovella<sup>18</sup>, E. Pearson<sup>18</sup>, C.U. Perez<sup>18,s</sup>, P. Rumerio<sup>18,t</sup>, R. Yi<sup>18</sup>, C. Cosby<sup>19</sup>, Z. Demiragli<sup>19</sup>, D. Gastler<sup>19</sup>, E. Hazen<sup>19</sup>, J. Rohlf<sup>19</sup>, E. Wurtz<sup>19</sup>, M. Hadley<sup>20</sup>, T. Kwon<sup>20</sup>, G. Landsberg<sup>20</sup>, K.T. Lau<sup>20</sup>, M. Stamenkovic<sup>20</sup>, X. Yan<sup>20,u</sup>, D.R. Yu<sup>20,v</sup>, A. Apresyan<sup>21</sup>, S. Banerjee<sup>21,w</sup>, F. Chlebana<sup>21</sup>, G. Cummings<sup>21</sup>, Y. Feng<sup>21,x</sup>, J. Freeman<sup>21</sup>, D. Green<sup>21,d</sup>, J. Hirschauer<sup>21</sup>, U. Joshi<sup>21</sup>, K.H.M. Kwok<sup>21</sup>, D. Lincoln<sup>21</sup>, S. Los<sup>21</sup>, C. Madrid<sup>21,x</sup>, N. Pastika<sup>21</sup>, K. Pedro<sup>21</sup>, S. Tkaczyk<sup>21</sup>, V. Hagopian<sup>22,†</sup>, T. Kolberg<sup>22</sup>, G. Martinez<sup>22</sup>, M. Alhusseini<sup>23</sup>, B. Bilki<sup>23,y</sup>, D. Blend<sup>23</sup>, P. Debbins<sup>23</sup>, K. Dilsiz<sup>23,z</sup>, L. Emediato<sup>23</sup>, F.D. Ingram<sup>23</sup>, O.K. Köseyan<sup>23</sup>, J.-P. Merlo<sup>23</sup>, A. Mestvirishvili<sup>23,aa</sup>, M. Miller<sup>23</sup>, H. Ogul<sup>23,bb</sup>, Y. Onel<sup>23</sup>, A. Penzo<sup>23</sup>, I. Schmidt<sup>23</sup>, D. Southwick<sup>23</sup>, E. Tiras<sup>23,cc</sup>, J. Wetzel<sup>23</sup>, L.F. Alcerro Alcerro<sup>24</sup>, S. Artega Escatell<sup>24</sup>, J. Bowen<sup>24,dd</sup>, M.R. Chukwuka<sup>24</sup>, C. Le Mahieu<sup>24</sup>, J. Marquez<sup>24</sup>, J. Mbagwu<sup>24</sup>, M. Murray<sup>24</sup>, M. Nickle<sup>24</sup>, S. Popescu<sup>24</sup>, C. Smith<sup>24</sup>, N. Islam<sup>25</sup>, K. Kaadze<sup>25</sup>, D. Kim<sup>25</sup>, Y. Maravin<sup>25</sup>, J. Natoli<sup>25</sup>, D. Roy<sup>25</sup>, R.D. Taylor<sup>25</sup>, A. Baden<sup>26</sup>, A. Belloni<sup>26</sup>, J. Bistany-riebman<sup>26</sup>, A. Bussio<sup>26</sup>, Y.M. Chen<sup>26</sup>, S.C. Eno<sup>26</sup>, T. Grassi<sup>26</sup>, N.J. Hadley<sup>26,d</sup>, R.G. Kellogg<sup>26,d</sup>, T. Koeth<sup>26</sup>, B. Kronheim<sup>26</sup>, Y. Lai<sup>26</sup>, S. Lascio<sup>26</sup>, A.C. Mignerey<sup>26</sup>, S. Nabili<sup>26</sup>, C. Palmer<sup>26</sup>, C. Papageorgakis<sup>26</sup>, M.M. Paranjpe<sup>26</sup>, E. Popova<sup>26,a</sup>, M. Seidel<sup>26,ee</sup>, A. Skuja<sup>26</sup>, L. Wang<sup>26</sup>, H. Bossi<sup>27</sup>, M. D'Alfonso<sup>27</sup>, G.M. Innocenti<sup>27</sup>, M. Klute<sup>27</sup>, J. Krupa<sup>27</sup>, M. Hu<sup>27</sup>, J. Lang<sup>27</sup>, C. McGinn<sup>27</sup>, B. Crossman<sup>28</sup>, C. Kapsiak<sup>28</sup>, M. Krohn<sup>28</sup>, J. Mans<sup>28</sup>, M. Revering<sup>28</sup>, N. Strobbe<sup>28</sup>, A. Das<sup>29</sup>, A. Heering<sup>29</sup>, N. Loukas<sup>29</sup>, J. Mariano<sup>29</sup>, Y. Musienko<sup>29,a</sup>, R. Ruchti<sup>29</sup>, M. Wayne<sup>29</sup>, A.D. Benaglia<sup>30</sup>, W. Chung<sup>30</sup>, S. Hoienko<sup>30</sup>, K. Kennedy<sup>30</sup>, G. Kopp<sup>30</sup>, T. Medvedeva<sup>30</sup>, K. Mei<sup>30</sup>, C. Tully<sup>30</sup>, O. Bessidskaia Bylund<sup>31</sup>, A. Bodek<sup>31</sup>, P. de Barbaro<sup>31</sup>, A. Garcia-Bellido<sup>31</sup>, A. Khukhunaishvili<sup>31</sup>, N. Parmar<sup>31</sup>, P. Parygin<sup>31,a</sup>, C.L. Tan<sup>31</sup>, R. Taus<sup>31</sup>, B. Chiarito<sup>32</sup>, J.P. Chou<sup>32</sup>, S.A. Thayer<sup>32</sup>, H. Wang<sup>32</sup>, N. Akchurin<sup>33</sup>, N. Gogate<sup>33</sup>, J. Damgov<sup>33</sup>, S. Kunori<sup>33</sup>, K. Lamichhane<sup>33</sup>, S.W. Lee<sup>33</sup>, S. Magedov<sup>33</sup>, A. Menkel<sup>33</sup>, S. Undleeb<sup>33</sup>, I. Volobouev<sup>33</sup>, H. Chung<sup>34</sup>, S. Goadhouse<sup>34</sup>, J. Hakala<sup>34</sup>, R. Hirosky<sup>34</sup>, V. Alexakhin<sup>35</sup>, V. Andreev<sup>35</sup>, Yu. Andreev<sup>35</sup>, T. Aushev<sup>35</sup>, M. Azarkin<sup>35</sup>, A. Belyaev<sup>35</sup>, S. Bitioukov<sup>35,†</sup>, E. Boos<sup>35</sup>, K. Bukin<sup>35</sup>, O. Bychkova<sup>35</sup>, M. Chadeeva<sup>35,a</sup>, R. Chistov<sup>35,a</sup>, M. Danilov<sup>35,a</sup>, A. Demianov<sup>35</sup>, A. Dermenev<sup>35</sup>, M. Dubinin<sup>35,ff</sup>, L. Dudko<sup>35</sup>, D. Elumakhov<sup>35</sup>, Y. Ershov<sup>35</sup>, A. Ershov<sup>35</sup>, V. Gavrillov<sup>35</sup>, I. Golutvin<sup>35,†</sup>, N. Gorbunov<sup>35</sup>, A. Gribushin<sup>35,a</sup>, A. Kaminskiy<sup>35</sup>, V. Karjavine<sup>35</sup>, A. Karneyev<sup>35</sup>, L. Khein<sup>35</sup>, M. Kirakosyan<sup>35</sup>, V. Klyukhin<sup>35,a</sup>, O. Kodolova<sup>35,gg</sup>, N. Krasnikov<sup>35</sup>, V. Krychkin<sup>35,†</sup>, A. Kurenkov<sup>35</sup>, N. Lychkovskaya<sup>35</sup>, V. Makarenko<sup>35,gg</sup>, P. Mandrik<sup>35</sup>, P. Moiseev<sup>35,†</sup>, V. Mossolov<sup>35,gg</sup>, S. Obraztsov<sup>35</sup>, A. Oskin<sup>35</sup>, V. Petrov<sup>35</sup>, S. Petrushanko<sup>35,a</sup>, S. Polikarpov<sup>35,a</sup>, V. Rusinov<sup>35</sup>, R. Ryutin<sup>35</sup>, V. Savrin<sup>35</sup>, D. Selivanova<sup>35</sup>, V. Smirnov<sup>35</sup>, A. Snigirev<sup>35</sup>, A. Sobol<sup>35</sup>, E. Tarkovskii<sup>35</sup>, A. Terkulov<sup>35</sup>, D. Tlisov<sup>35,†</sup>, I. Tlisova<sup>35</sup>, R. Tolochech<sup>35</sup>, M. Toms<sup>35,hh</sup>, A. Toropin<sup>35</sup>, S. Troshin<sup>35</sup>, A. Volkov<sup>35</sup>, P. Volkov<sup>35</sup>, B. Yuldashev<sup>35,†</sup>, A. Zharbin<sup>35</sup>, A. Zhokin<sup>35</sup>

<sup>1</sup>University of Agder, Grimstad, Norway\*

<sup>2</sup>Yerevan Physics Institute, Yerevan, Armenia

<sup>3</sup>Department of Physics, University of Cyprus, Nicosia, Cyprus

<sup>4</sup>National Technical University of Athens, Athens, Greece

<sup>5</sup>Deutsches Elektronen-Synchrotron, Hamburg, Germany\*

<sup>6</sup>MTA-ELTE Lendület CMS Particle and Nuclear Physics Group, Eötvös Loránd University, Budapest, Hungary

<sup>7</sup>Saha Institute of Nuclear Physics, Kolkata, India\*

<sup>8</sup>Tata Institute of Fundamental Research-B, Mumbai, India

<sup>9</sup>National Institute of Science Education and Research, Odisha, India\*

<sup>10</sup>Korea University, Seoul, Korea

<sup>11</sup>Çukurova University, Physics Department, Science and Art Faculty, Adana, Turkey

<sup>12</sup>Bogazici University, Istanbul, Turkey

<sup>13</sup>Istanbul Technical University, Istanbul, Turkey

<sup>14</sup>Yildiz Technical University, Istanbul, Turkey

<sup>15</sup>Istanbul University, Istanbul, Turkey

<sup>16</sup>National Science Centre, Kharkiv Institute of Physics and Technology, Kharkiv, Ukraine

<sup>17</sup>Baylor University, Waco, Texas, USA

<sup>18</sup>The University of Alabama, Tuscaloosa, Alabama, USA

<sup>19</sup>Boston University, Boston, Massachusetts, USA

<sup>20</sup>Brown University, Providence, Rhode Island, USA

<sup>21</sup>Fermi National Accelerator Laboratory, Batavia, Illinois, USA

- 
- <sup>22</sup>Florida State University, Tallahassee, Florida, USA  
<sup>23</sup>The University of Iowa, Iowa City, Iowa, USA  
<sup>24</sup>The University of Kansas, Lawrence, Kansas, USA  
<sup>25</sup>Kansas State University, Manhattan, Kansas, USA  
<sup>26</sup>University of Maryland, College Park, Maryland, USA  
<sup>27</sup>Massachusetts Institute of Technology, Cambridge, Massachusetts, USA  
<sup>28</sup>University of Minnesota, Minneapolis, Minnesota, USA  
<sup>29</sup>University of Notre Dame, Notre Dame, Indiana, USA  
<sup>30</sup>Princeton University, Princeton, New Jersey, USA  
<sup>31</sup>University of Rochester, Rochester, New York, USA  
<sup>32</sup>Rutgers, The State University of New Jersey, Piscataway, New Jersey, USA  
<sup>33</sup>Texas Tech University, Lubbock, Texas, USA  
<sup>34</sup>University of Virginia, Charlottesville, Virginia, USA  
<sup>35</sup>Authors affiliated with an institute or an international laboratory covered by a cooperation agreement with CERN

\*No longer in CMS HCAL Collaboration

‡: Deceased

<sup>a</sup> Also at an institute or an international laboratory covered by a cooperation agreement with CERN

<sup>b</sup> Also at HUN-REN Wigner Research Centre for Physics, Budapest, Hungary

<sup>c</sup> Now at Indian Institute of Technology Madras, Chennai, India

<sup>d</sup> Emeritus

<sup>e</sup> Now at Indian Institute of Science, Bangalore, India

<sup>f</sup> Also at Near East University, Research Center of Experimental Health Science, Nicosia, Turkey

<sup>g</sup> Also at Konya Technical University, Konya, Turkey

<sup>h</sup> Also at Bakircay University, Izmir, Turkey

<sup>i</sup> Also at Adiyaman University, Adiyaman, Turkey

<sup>j</sup> Also at Marmara University, Istanbul, Turkey

<sup>k</sup> Also at Milli Savunma University, Istanbul, Turkey

<sup>l</sup> Also at Kafkas University, Kars, Turkey

<sup>m</sup> Also at Istanbul Bilgi University, Istanbul, Turkey

<sup>n</sup> Also at Hacettepe University, Ankara, Turkey

<sup>o</sup> Also at Mimar Sinan Fine Arts University, Istanbul, Turkey

<sup>p</sup> Also at Istinye University, Istanbul, Turkey

<sup>q</sup> Also at Bogazici University, Istanbul, Turkey

<sup>r</sup> Also at Istanbul University–Cerrahpasa, Faculty of Engineering, Istanbul, Turkey

<sup>s</sup> Now at Universitat Ramon Llull, Barcelona, Spain

<sup>t</sup> Also at Università di Torino, Torino, Italy

<sup>u</sup> Now at University of California, Santa Barbara, USA

<sup>v</sup> Now at State University of New York, Buffalo, USA

<sup>w</sup> Now at University of Wisconsin-Madison, Madison, USA

<sup>x</sup> Now at Texas Tech University, Lubbock, USA

<sup>y</sup> Also at Beykent University, Istanbul, Turkey

<sup>z</sup> Also at Bingol University, Bingol, Turkey

<sup>aa</sup> Also at Georgian Technical University, Tbilisi, Georgia

<sup>bb</sup> Also at Sinop University, Sinop, Turkey

<sup>cc</sup> Also at Erciyes University, Kayseri, Turkey

<sup>dd</sup> Now at Baker University, Baldwin City, USA

<sup>ee</sup> Now at Riga Technical University, Riga, Latvia

<sup>ff</sup> Also at California Institute of Technology, Pasadena, California, USA

<sup>gg</sup> Now at Yerevan Physics Institute, Yerevan, Armenia

<sup>hh</sup> Now at Karlsruhe Institute of Technology, Karlsruhe, Germany